PHYSICAL REVIEW D **91,** 084011 (2015)

Discovering the QCD axion with black holes and gravitational waves

Asimina Arvanitaki[*]
Perimeter Institute for Theoretical Physics, Waterloo, Ontario N2L 2Y5, Canada

Masha Baryakhtar[†] and Xinlu Huang[‡]
Stanford Institute for Theoretical Physics, Department of Physics, Stanford University, Stanford, California 94305, USA

(Received 16 December 2014; published 7 April 2015)

Advanced LIGO may be the first experiment to detect gravitational waves. Through superradiance of stellar black holes, it may also be the first experiment to discover the QCD axion with decay constant above the grand unification scale. When an axion's Compton wavelength is comparable to the size of a black hole, the axion binds to the black hole, forming a "gravitational atom." Through the superradiance process, the number of axions occupying the bound levels grows exponentially, extracting energy and angular momentum from the black hole. Axions transitioning between levels of the gravitational atom and axions annihilating to gravitons can produce observable gravitational wave signals. The signals are long lasting, monochromatic, and can be distinguished from ordinary astrophysical sources. We estimate up to $\mathcal{O}(1)$ transition events at aLIGO for an axion between 10^{-11} and 10^{-10} eV and up to 10^4 annihilation events for an axion between 10^{-13} and 10^{-11} eV. In the event of a null search, aLIGO can constrain the axion mass for a range of rapidly spinning black hole formation rates. Axion annihilations are also promising for much lighter masses at future lower-frequency gravitational wave observatories; the rates have large uncertainties, dominated by supermassive black hole spin distributions. Our projections for aLIGO are robust against perturbations from the black hole environment and account for our updated exclusion on the QCD axion of 6×10^{-13} eV $< \mu_a < 2 \times 10^{-11}$ eV suggested by stellar black hole spin measurements.

DOI: 10.1103/PhysRevD.91.084011 PACS numbers: 04.30.Db, 04.30.-w, 97.60.Lf, 14.80.−j

I. WHAT IS SUPERRADIANCE?

A wave that scatters from a rotating black hole can exit the black hole environment with a larger amplitude than the one with which it came in. This amplification happens for both matter and light waves and it is called black hole superradiance. It is an effect that has been known for nearly 50 years [1].

Massive bosonic waves are special. They form bound states with the black hole whose occupation number can grow exponentially [2]; for fermions, Pauli's exclusion principle makes this lasing effect impossible. This exponential growth is understood if one considers the mass of the boson acting as a mirror that forces the wave to confine in the black hole's vicinity and to scatter and superradiate continuously. This is known as the superradiance (SR) instability for a Kerr black hole and is an efficient method of extracting angular momentum and energy from the black hole. Rapidly spinning astrophysical black holes thus become a diagnostic tool for the existence of light massive bosons [3,4].

Black hole superradiance sounds exotic and mysterious since it naively appears to be deeply connected with nonlinear gravitational effects in the vicinity of black holes. Instead, superradiance is a purely kinematic effect, and black hole superradiance is just another manifestation of the superradiance phenomenon that appears in a variety of systems. The most famous is inertial motion superradiance, most commonly referred to as Cherenkov radiation [5]. In Cherenkov radiation, a nonaccelerating charged particle spontaneously emits radiation while moving superluminally in a medium. The emitted radiation forms a cone with opening angle $\cos\theta = (nv)^{-1}$, where n is the index of refraction of the medium, and radiation that scatters inside the cone $(\omega_\gamma < \vec{v} \cdot \vec{k}_\gamma)$ is amplified [6].

Similarly, superradiance occurs for a conducting axisymmetric body rotating at a constant angular velocity Ω_{cylinder} [7]. Here, superluminal motion is in the angular direction: a rotating conducting cylinder amplifies any light wave of the form $e^{im\varphi - i\omega_\gamma t}$ when the rotational velocity of the cylinder is faster than the angular phase velocity of the light:

$$\frac{\omega_\gamma}{m} < \Omega_{\text{cylinder}}, \tag{1}$$

where ω_γ and m are the photon energy and angular momentum with respect to the cylinder rotation axis, respectively. This is the same as the superradiance condition for rotating black holes, with Ω_{cylinder} substituted by the

[*]aarvanitaki@perimeterinstitute.ca
[†]mbaryakh@stanford.edu
[‡]xinluh@stanford.edu

angular velocity of the black hole at the horizon. The only difference is in the (dissipative) interaction required for superradiance to occur: in the case of a conducting cylinder, it is electromagnetism, while for black holes, it is gravity.

Although the kinematic condition is easy to satisfy, the amplification rate is typically small, and rotational superradiance in particular is very hard to observe. The amplification rate is determined by the overlap of the scattered wave with the rotating object; for nonrelativistic rotation, this overlap is proportional to $(\omega_\gamma R)^{2m}$ where R is the size of the object. The superradiance condition in Eq. (1) implies that this quantity is generically much less than 1. As Bekenstein notes, only superradiance for the $m = 1$ mode could potentially be observed in the lab [6]. For black holes, however, several modes with $m \geq 1$ can be superradiating within the evolution time scale of the black hole since their rotation is relativistic.

The smallness of the superradiance rate also highlights the importance of axisymmetry. For nonaxisymmetric objects, SR modes mix with non-SR (decaying) ones, and hence the amplification rate is even smaller or nonexistent. This is another complication for observing rotational superradiance in the lab as well as around astrophysical objects such as stars and planets.

To summarize, rotating black holes are just one type of system in which superradiance can occur. However, they have special properties that make them ideal for observing superradiance of massive bosonic particles:

(i) They are perfectly axisymmetric due to the no-hair theorem.
(ii) Their rotation is relativistic so the SR rate can be significant.
(iii) Gravity provides the interaction necessary for SR to occur, so the effect is universal for all particles.

In particular, the superradiance rate for black holes can be significantly faster than the dynamical black hole evolution rate. It is maximized when the Compton wavelength of the massive bosonic particle is comparable to the black hole size: astrophysical black holes are sensitive detectors of bosons with masses between 10^{-20} and 10^{-10} eV.

This mass range encompasses many theoretically motivated light bosons. In particular, the QCD axion, a pseudo-Goldstone boson proposed to solve the strong CP problem [8], falls in this mass range for high decay constant $f_a \simeq 10^{17}$ GeV$(6 \times 10^{-11}$ eV$/\mu_a)$, where μ_a is the axion mass. Many light axions can also arise in the landscape of string vacua [3]. Other classes of particles probed by superradiance include light dilatons [9] and light gauge bosons of hidden $U(1)$s (see [10] and references therein). Black hole superradiance can probe parameter space that is inaccessible to laboratories or astrophysics since naturally light bosons have small or no couplings to the standard model.

As long as the self-interaction of the boson is sufficiently weak and its Compton wavelength comparable to the size of astrophysical black holes, superradiance will operate, regardless of the model or the abundance of the boson. We mostly refer to the QCD axion, but our result is directly applicable to general scalars via $\lambda \leftrightarrow (\mu_a/f_a)^2$ for a scalar with mass μ_a and quartic interaction $\mathcal{L} \supset \lambda\phi^4/4!$. The same results can also be approximately applied to light vector bosons.

When the superradiance effect is maximized, a macroscopic "cloud" of particles forms around the black hole, giving dramatic experimental signatures [4]. The signals are sizable even after taking into account bounds suggested by measurements of rapidly spinning black holes, which would have spun down quickly in the presence of light bosonic particles of appropriate masses.

Black hole superradiance is fast enough to allow multiple levels to superradiate within the dynamical evolution time scale of astrophysical black holes. Axions occupying these levels can annihilate to a single graviton in the presence of the black hole's gravitational field. Levels with the same angular momentum quantum numbers but different energies can be simultaneously populated; axions that transition between them emit gravitational radiation. As we will see, both axion transitions and annihilations produce monochromatic gravitational wave radiation of appreciable intensity. The gravitational wave frequency and strain for grand unification scale to Planck-scale QCD axions fall in the optimal sensitivity band for Advanced LIGO (aLIGO) [11] and VIRGO [12].

The annihilations signature is also promising at future, low-frequency gravitational wave observatories. Another signal relevant for bosons with self-coupling stronger than the QCD axion is the "bosenova" effect [4], where the bosonic cloud collapses under its self-interactions, producing periodic gravitational wave bursts.

In this paper, we focus on the prospects for detecting gravitational wave signals at aLIGO and discuss the reach for future gravitational wave detectors operating at lower frequencies. In Sec. II, we review the parameters for black hole superradiance and how it evolves for an astrophysical black hole. In Sec. III, we estimate expected event rates at aLIGO and at future lower frequency detectors. In Sec. IV, we revisit bounds from black hole spin measurements and include our results for both stellar and supermassive black holes. We examine the effects of black hole companion stars and accretion disks on superradiance in Sec. V, and conclude in Sec. VI.

II. THEORETICAL BACKGROUND

A. The gravitational atom in the sky

The bound states of a massive boson with the black hole (BH) are closely approximated by hydrogen wave functions: except in very close proximity to the black hole, the gravitational potential is $\propto 1/r$. The "fine-structure constant" α of the gravitational atom is

$$\alpha = r_g \mu_a, \qquad r_g \equiv G_N M, \tag{2}$$

where r_g is the gravitational radius of the BH, M its mass, and μ_a the boson's mass. Throughout this paper, we use units where $c = \hbar = 1$. Like the hydrogen atom, the orbitals around the black hole are indexed by the principal, orbital, and magnetic quantum numbers $\{n, \ell, m\}$ with energies:

$$\omega \simeq \mu_a \left(1 - \frac{\alpha^2}{2n^2}\right). \tag{3}$$

The orbital velocity is approximately $v \sim \alpha/\ell$, and the axions form a cloud with average distance

$$r_c \sim \frac{n^2}{\alpha^2} r_g \tag{4}$$

from the black hole.

A level with energy ω and magnetic quantum number m can extract energy and angular momentum from the black hole if it satisfies the superradiance condition analogous to Eq. (1):

$$\frac{\omega}{m} < \omega^+, \qquad \omega^+ \equiv \frac{1}{2}\left(\frac{a_*}{1+\sqrt{1-a_*^2}}\right) r_g^{-1}, \tag{5}$$

where ω^+ can be thought of as the angular velocity of the black hole and $0 \le |a_*| < 1$ is the black hole spin ($a_* \equiv a/r_g$ in Boyer-Lindquist coordinates). The SR condition requires

$$\alpha/\ell \le 1/2, \tag{6}$$

with the upper bound saturated for $m = \ell$ and extremal black holes ($a_* = 1$), so superradiating bound states are indeed well approximated by solutions to a $1/r$ gravitational potential ($r_c \gg r_g$) with subleading relativistic corrections ($v^2 \ll 1$).

The occupation number[1] N of levels that satisfy the SR condition grows exponentially with a rate $\Gamma_{\rm sr}$,

$$\left.\frac{dN}{dt}\right|_{\rm sr} = \Gamma_{\rm sr} N,$$
$$\Gamma_{\rm sr}^{n\ell m}(a_*, \alpha, r_g) = \mathcal{O}(10^{-7}\text{–}10^{-14}) r_g^{-1}. \tag{7}$$

The boson is not required to be dark matter or be physically present in the vicinity of the black hole: just like spontaneous emission, superradiance can start by a quantum mechanical fluctuation from the vacuum, and proceed to grow exponentially. If the SR condition is satisfied, the growth will occur as long as the rate is faster than the evolution time scales of the BH, the most relevant of which is the Eddington accretion time, $\tau_{\rm Eddington} = 4 \times 10^8$ years. The growth stops when enough angular momentum has been extracted so that the superradiance condition is no longer satisfied. At that point the number of bosons occupying the level is

$$N_{\rm max} \simeq \frac{G_N M^2}{m} \Delta a_* \sim 10^{76} \left(\frac{\Delta a_*}{0.1}\right)\left(\frac{M}{10 M_\odot}\right)^2, \tag{8}$$

where $\Delta a_* = \mathcal{O}(0.1)$ is the difference between the initial and final BH spin.

The superradiance rates (or dumping rates for the levels that are not superradiating) are given by the small imaginary part of the energy of a free-field solution in the Kerr background. Unless otherwise specified, we use the semi-analytic approach for massive spin-0 fields presented in [4], which agrees well with analytical formulas for $\alpha/\ell \ll 1$ [2] and the WKB approximation for $\alpha/\ell \sim \mathcal{O}(1/2)$ [2,4], as well as with partial numerical results in [13]. Rates for massive spin-1 fields are expected to be larger, and some numerical progress has been made toward calculating them [14]; we choose to focus on the spin-0 case (including the QCD axion) for the remainder of this paper, but further studies with spin-1 fields are very worthwhile.

In Fig. 1 we show representative values of the superradiance rates, $\Gamma_{\rm sr}$, and we list sample values in Table I along with typical BH evolution time scales. The rate varies with the relevant parameters of the system as follows:

(i) r_g.—The dimensionless quantity $\Gamma_{\rm sr} r_g$ depends only on the coupling α, BH spin a_* and the quantum numbers of the state; the physical SR time can be as short as 100 s for stellar black holes and is longer for heavier black holes.

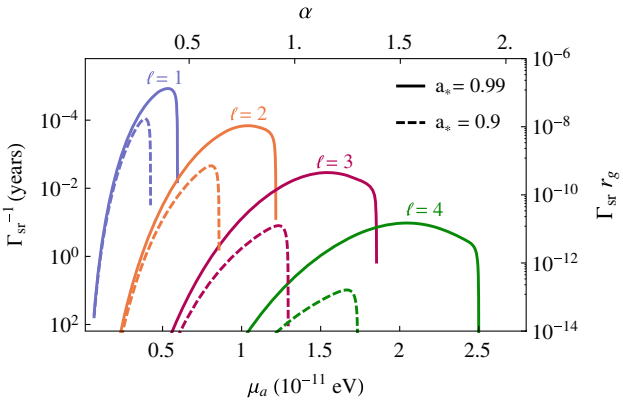

FIG. 1 (color online). Superradiance times of levels $\ell = 1$ to 4 (left to right) for spins $a_* = 0.99$ and 0.90, fixing $m = \ell$ and $n = \ell + 1$. Time in years is shown for a $10 M_\odot$ black hole as a function of boson mass μ_a; on the right axis, we show the dimensionless superradiance rate $\Gamma_{\rm sr} r_g$ as a function of the gravitational coupling α (top axis).

[1]The axion cloud surrounding the BH is described by a classical field, and therefore does not have a well-defined occupation number N. In this paper we define the occupation number as the average value of bosons in the cloud.

(ii) α.—For given level, Γ_{sr} is a steep function of the coupling, reaching its maximum close to the SR boundary. A single BH is sensitive to a range of boson masses: stellar BHs (2–$100M_\odot$) correspond to masses of 10^{-13}–10^{-10} eV, and supermassive BHs (10^6–$10^8 M_\odot$) to masses of 10^{-19}–10^{-16} eV.

(iii) a_*.—The dependence of Γ_{sr} on spin enters primarily through the SR condition. The upper bound on α/ℓ becomes smaller than $1/2$ for lower spin BHs, and the maximum SR rate is thus smaller than for equivalent BHs with higher spins.

(iv) ℓ.—Γ_{sr} decreases with increasing ℓ, and the dependence is strong: for $\alpha/\ell \ll 1$, $\Gamma_{sr} \propto \alpha^{4\ell}$ [2], while for $\alpha/\ell \sim 0.5$, the WKB approximation [2,4] gives $\Gamma_{sr} \propto e^{-3.7\alpha} = (0.15)^\ell$.

(v) m.—Γ_{sr} is largest for $m = \ell$ and is much smaller for $m < \ell$. Unless otherwise specified, we only consider levels with $m = \ell$ below.

(vi) n.—For fixed ℓ and m, the dependence on n is mild and Γ_{sr} generally decreases with larger n.

So far, we have considered a free bosonic field. Self-interactions between bosons will affect superradiance when the interaction energy becomes comparable to the binding energy of the boson in the cloud [4]. Axions, for example, have attractive self-interactions which cause the cloud to collapse when it reaches a critical size; laboratory experiments have observed such collapse of bosonic states, known as bosenova, in the analogous system of trapped Bose–Einstein condensates [15]. Bosenovae can even be a portal into a hidden sector to which a generalized light axion couples [16]. After a bosenova occurs, the superradiant growth restarts. Even weak self-interactions can have a significant effect: for example, for an axion with decay constant f_a, the critical bosenova occupation number is

$$N_{\rm bosenova} \simeq 10^{78} c_0 \frac{n^4}{\alpha^3} \left(\frac{M}{10M_\odot}\right)^2 \left(\frac{f_a}{M_{\rm pl}}\right)^2, \qquad (9)$$

where $M_{\rm pl} = 2 \times 10^{18}$ GeV and $c_0 \sim 5$ is determined by numerical simulation [17]. Comparing Eqs. (8) and (9), we see that the bosenova occurs before all the spin is extracted when

$$f_a \lesssim 2 \times 10^{16}\ {\rm GeV} \frac{1}{\sqrt{n}} \left(\frac{\alpha/n}{0.4}\right)^{\frac{3}{2}} \left(\frac{\Delta a_*}{0.1}\right)^{\frac{1}{2}} \left(\frac{5}{c_0}\right)^{\frac{1}{2}}. \qquad (10)$$

For the QCD axion this gives $\mu_a > 3 \times 10^{-10}$ eV, too heavy to be relevant for astrophysical black holes ($M \gtrsim 3M_\odot$). Nevertheless, the bosenova can lead to interesting gravitational wave signals for axionlike particles and other light bosons (Sec. III C). For strongly interacting bosons, the superradiance instability can be slowed to a stand-still with the cloud collapsing before it can grow to macroscopic size.

In this section, we use the results of [2,4]; we refer readers to these references for further details. For a broad review of SR, see [18].

B. A (not so) brief history of superradiance

The superradiance condition can be satisfied for several levels of the black hole-axion "atom," and for each level and boson mass, there is a region in the BH spin vs mass plane that is affected (Fig. 2). As discussed previously, the superradiance condition is a kinematic one and SR can affect BHs with masses a factor of 10 to 100 around the optimal value. The affected region is set by the SR condition and is further limited by whether superradiance happens faster than the accretion rate of the BH.

In order to understand how superradiance affects astrophysical black holes, let us assume there exists a boson with mass $\mu_a = 10^{-11}$ eV and self-interaction strength of the QCD axion (decay constant $f_a = 6 \times 10^{17}$ GeV). The Compton wavelength of this particle is 20 km, the size of a typical stellar BH horizon.

Consider a BH that is born with spin $a_* = 0.95$ and mass $6M_\odot$. Once the environment settles to a steady state after the supernova explosion, superradiant levels begin to grow exponentially with their respective SR rates. The fastest-growing level dominates—in this case, the $\ell = 2$ level, since the smallest ℓ that satisfies the SR condition has the largest rate. It takes $\log N_{\rm max} \sim 200$ e-folds—in this case, about 2 years—of growth to extract enough spin so that the SR condition is no longer satisfied for the $\ell = 2$ level. While losing 20% of the spin, the BH only loses about 5% of its mass, because the cloud is larger in extent than the black hole and so more efficient at carrying angular momentum [4]. As the cloud grows, the gravitational wave signal from axion annihilation (Sec. III B) increases until

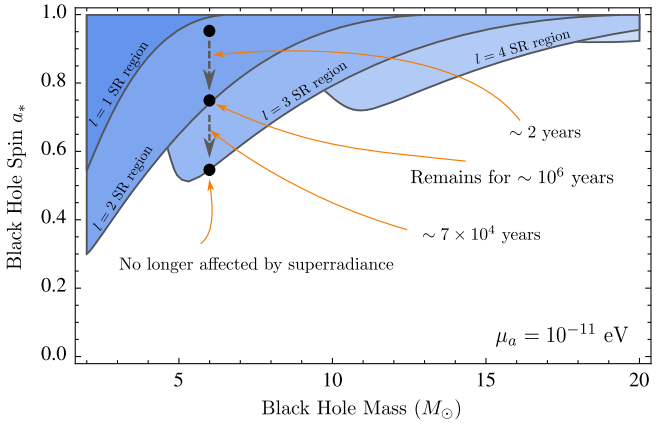

FIG. 2 (color online). Effect of superradiance for a QCD axion with mass $\mu_a = 10^{-11}$ eV and decay constant $f_a = 6 \times 10^{17}$ GeV. Shaded regions correspond to BH parameters which would result in spin-down within a binary lifetime (10^6 years), for $\ell = 1$ (dark blue) to $\ell = 5$ (light blue) levels. We also show an example evolution of a $6M_\odot$ black hole with initial spin $a_* = 0.95$.

TABLE I. Characteristic superradiance time scales. We use $10M_\odot$ and $10^7 M_\odot$ as representative stellar and supermassive black hole masses. The $2p$ level is the most relevant for annihilation signals, and the $5g$ level for transition signals.

Process		(see also)	Stellar BHs	Supermassive BHs
Superradiance $(2p, \alpha = 0.3, a_* = 0.9)$	$\Gamma_{\rm sr}^{-1}$	Fig. 1	10^{-4} yr	100 yr
Superradiance $(5g, \alpha = 1.2, a_* = 0.9)$	$\Gamma_{\rm sr}^{-1}$	Fig. 1	10 yr	10^7 yr
Regge trajectory $(2p, \alpha = 0.3, f_a = 10^{17}$ GeV)	$\tau_{\rm regge}$	Eq. (11)	10^6 yr	10^{12} yr
Eddington Accretion, $(\dot{M}/M)^{-1}$	$\tau_{\rm eddington}$		4×10^8 yr	4×10^8 yr

reaching a maximum when the SR condition is no longer satisfied.

At this point, we expect superradiance to start populating the $\ell = 3$ at a slower rate. If self-interactions are present, this does not happen right away: the $\ell = 2$ level perturbs the potential around the black hole such that the $\ell = 3$ level mixes with levels that do not satisfy the SR condition. Therefore the $\ell = 3$ level does not grow until the $\ell = 2$ level is depleted to the point when level mixing is a subdominant effect. The time scale for the ℓth level to be depleted sufficiently is dominated by two-boson to one graviton annihilations [4],

$$\tau_{\rm regge} \simeq (N_{\rm bosenova}\Gamma_a)^{-1} |\Gamma_{\rm sr}^{\ell-1}/\Gamma_{\rm sr}^{\ell+1}|^{1/2}, \qquad (11)$$

where Γ_a is the annihilation rate (Sec. III B). For interacting particles $\tau_{\rm regge}$ can be much longer than the superradiance time since $(N_{\rm bosenova}\Gamma_a) < \Gamma_{\rm sr}$ and $|\Gamma_{\rm sr}^{\ell-1}/\Gamma_{\rm sr}^{\ell+1}|^{1/2} \gg 1$. The black hole can therefore spend a long time on the line where $\omega = m\omega_+$. This line thus defines for black holes the analog of Regge trajectories in particle physics. If black hole spin measurements become accurate enough, we could diagnose the presence of an axion by fitting the curve of BH spin vs mass to the superradiance condition.

Once the $\ell = 2$ level is depleted through annihilations, the $\ell = 3$ level starts to grow and the BH makes another jump in the BH spin vs mass plane. The previous process then repeats itself, but for the parameters chosen, the $\ell = 4$ superradiance rate is too slow and once the spin drops to $a_* = 0.55$, superradiance no longer affects the BH.

If the black hole is heavier such that the $\ell = 4$ superradiance rate is significant, the $5g$ and $6g$ levels grow with comparable superradiance rates to large occupation numbers. This sets the stage for a large gravitational wave signal from level transitions (Sec. III A); $\ell = 4$ is the smallest ℓ for which significant transition signals occur.

The BH trajectory is more complicated if the bosenova is possible. In that case, the cloud reaches a maximum size of $N_{\rm bosenova}$ and collapses before saturating the superradiance condition. Then, the bosenova has to repeat many times before the superradiance condition is saturated, and the occupation number of the cloud at the Regge trajectory is smaller by a corresponding factor. As we discuss in Sec. III C, the periodic repetition of bosenovae can give rise to interesting signals.

For supermassive black holes the story changes slightly, since their spin and mass are acquired through accretion. As a supermassive BH grows, spin extraction by the cloud happens adiabatically with black hole accretion, moving the BH along the boundary of the region in the spin vs mass plane affected by superradiance. Only a violent event such as a merger will perturb the system enough so the BH can jump between different levels. The long time spent on the trajectories can lead to exciting annihilation signals at low-frequency gravitational wave detectors (Sec. III B 2).

III. GRAVITATIONAL WAVE SIGNALS

Processes that have forbiddingly small rates for a single particle can be enhanced in the bosonic cloud, since the occupation number of a single level in the BH-boson gravitational atom can be exponentially large. Transitions of bosons between two different levels are enhanced by $N_1 N_2$ where N_i is the occupation number for each level; two-boson annihilations to a single graviton are enhanced by N_i^2. Because of this "lasing" effect, the peak strain of the resulting gravitational waves (GW) can be within reach of GW detectors. Superradiance for stellar black holes can lead upcoming observatories, Advanced LIGO [11] and Advanced VIRGO [12]—beginning science runs in 2015–2016 [19]—into the realm of discovery. Superradiance for supermassive black holes has exciting prospects for future, low-frequency observatories.

There are three types of GW signals from the bosonic cloud:

(i) graviton emission from level transitions
(ii) axion annihilations into gravitons
(iii) bosenova collapse of the axion cloud.

The axions involved in transitions and annihilations are in exact energy eigenstates of the black hole potential and thus emit monochromatic GWs.[2] As the occupation number of a level changes, the axion energy receives a correction $\Delta E \sim E_{\rm bind} N/(2N_{\rm bosenova})$ due to axion self-interactions [4], leading to a small frequency drift of the emitted GW which can be used to distinguish the signal from astrophysical sources.

[2]This disagrees with what was stated in [4] regarding the monochromaticity of GWs from annihilations. We thank S. Dimopoulos and S. Dubovsky for discussions clarifying this issue.

TABLE II. Characteristic GW signal time scales and parameters. We use $10M_\odot$ and $10^7 M_\odot$ as representative stellar and supermassive black hole masses, and spin of $a_* = 0.9$. Signal length is defined as the duration for which signal is larger than $1/e$ of its maximum (see Secs. III A and III B).

		(see also)	Stellar BHs	Supermassive BHs
Transition ($6g \to 5g, \alpha = 1.2$)	Γ_t^{-1}	Eq. (16)	10^{72} yr	10^{90} yr
Annihilation ($2p$, $\alpha = 0.3$)	Γ_a^{-1}	Eq. (24)	10^{79} yr	10^{97} yr
Maximum number of axions in the cloud	$N_{\max}$	Eq. (8)	10^{76}	10^{88}
Transition signal length ($6g \to 5g, \alpha = 1.2$)	$\mathcal{O}(1) \times \Gamma_{\rm sr}^{-1}$	Fig. 3	5 yr	5×10^6 yr
Annihilation signal length ($2p, \alpha = 0.3$)	$(N_{\max}\Gamma_a)^{-1}$	Eq. (25)	10^3 yr	10^9 yr

In this section, we compute the experimental reach of GW observatories and estimate expected event rates. Table II summarizes the time scales typical for these processes. We focus on light axions as a prime example of bosons relevant for superradiance, since their mass and self-interaction are naturally small due to shift symmetry. When relevant, we assume the self-coupling is that of the QCD axion in this section.

To calculate the GW strain we use

$$h = \left(\frac{4G_N P}{r^2\omega^2}\right)^{1/2} \tag{12}$$

for a source emitting power P of angular frequency ω at a distance r away from the Earth. We do not include the effects from the angular dependence and orientation of the GW detectors.

We compare the signal strain to GW detector sensitivity $h_{\rm det}$ for a search with $N_{\rm seg}$ segments of $T_{\rm coh}$ coherent integration times:

$$h_{\rm det} = n(\sigma) C_{\rm tf} \frac{\sqrt{S_h}}{N_{\rm seg}^{1/4} T_{\rm coh}^{1/2}}, \tag{13}$$

where S_h is the detector noise spectral density, $n(\sigma)$ is the signal to noise ratio for a desired signal significance, and $C_{\rm tf}$ the trials factor. We use $C_{\rm tf} = 10$ in this section as a realistic value since we expect frequency drifts to be unimportant for this search [20] (compared to $C_{\rm tf} \sim 20$ in the current LIGO periodic gravitational wave search, where $H \simeq n(\sigma) N_{\rm seg}^{1/4} C_{\rm tf} \sim 150$ [21]).

A. Level transitions

Analogously to atomic transitions emitting photons, level transitions of axions around black holes emit gravitons. The GW angular frequency for transitions between an "excited" and a "ground" level with principal quantum numbers n_e and n_g, respectively, is

$$\omega_{\rm tr} = \frac{1}{2}\mu_a \alpha^2 \left(\frac{1}{n_g^2} - \frac{1}{n_e^2}\right). \tag{14}$$

When the two levels dominate the SR evolution, their occupation numbers $N_{e,g}$ evolve with their respective SR rates, modified by axions transitioning from the excited to the ground state via graviton emission,

$$\frac{dN_g}{dt} = \Gamma_g^{\rm sr} N_g + \Gamma_t N_g N_e, \qquad \frac{dN_e}{dt} = \Gamma_e^{\rm sr} N_e - \Gamma_t N_e N_g, \tag{15}$$

where $\Gamma_{g,e}^{\rm sr}$ are the superradiance rates for the two levels and Γ_t the transition rate for a single axion. A quadrupole formula estimate gives

$$\Gamma_t \sim \frac{2G_N\omega^5}{5}\mu_a^2 r_c^4 = \mathcal{O}(10^{-6}\text{–}10^{-8})\frac{G_N\alpha^9}{r_g^3}. \tag{16}$$

For our numerical results, we compute more precise rates (see Appendix A).

Although the single axion transition rate is tiny ($\Gamma_t \lll \Gamma_{e,g}^{\rm sr}$), the emission of gravitational waves is enhanced by the occupation numbers of each level:

$$h_{\rm tr}(t) = \sqrt{\frac{4G_N}{r^2\omega_{\rm tr}}\Gamma_t N_g(t) N_e(t)}. \tag{17}$$

When the axion clouds are small, transitions are negligible, and both levels grow exponentially with their respective SR rates. The transition terms in Eq. (15) become important when the transition rate starts to compete with the growth rate. The occupation number of the excited level is maximized when

$$N_g = \Gamma_e^{\rm sr}/\Gamma_t, \tag{18}$$

after which the excited state depopulates rapidly. The size of the signal depends on whether $\Gamma_e^{\rm sr} > \Gamma_g^{\rm sr}$ or vice versa. An example of the N_g, N_e and h time evolution for the two cases is shown in Fig. 3.

If $\Gamma_e^{\rm sr} > \Gamma_g^{\rm sr}$ (Fig. 3, left), $N_e \gg N_g$ at the time when the transition terms become relevant. The transition GW strain keeps growing as the excited level gets depleted, until both levels are populated with an equal number of axions. After that, the signal drops precipitously as the excited level empties out and the ground state returns to growing with rate $\Gamma_g^{\rm sr}$.

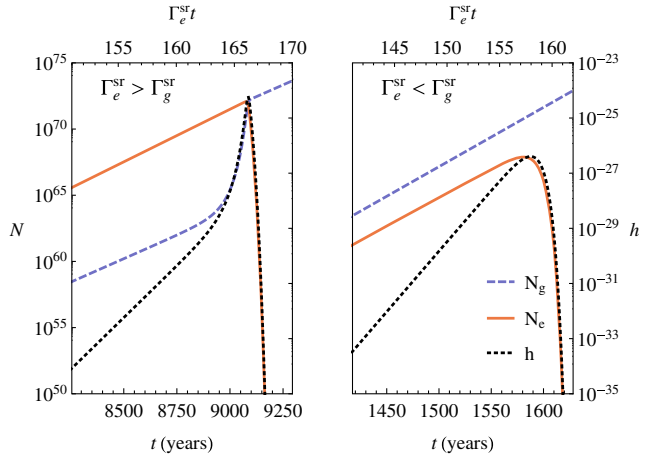

FIG. 3 (color online). Time evolution of ground and excited levels' occupation numbers (left y-axis) and the resulting gravitational wave signal strain (right y-axis) for the $6g \to 5g$ transition around a $10M_\odot$ black hole with spin $a_* = 0.9$, 10 kpc away. The peak signal is larger when $\Gamma_e > \Gamma_g$ (left, $\alpha = 1$) than the case $\Gamma_e < \Gamma_g$ (right, $\alpha = 1.25$). The initial occupation numbers of both levels are set to 1 when $t = 0$, and while the time in years differs significantly, the characteristic time scales for the signals are set by the superradiance rates (top axes) in both cases.

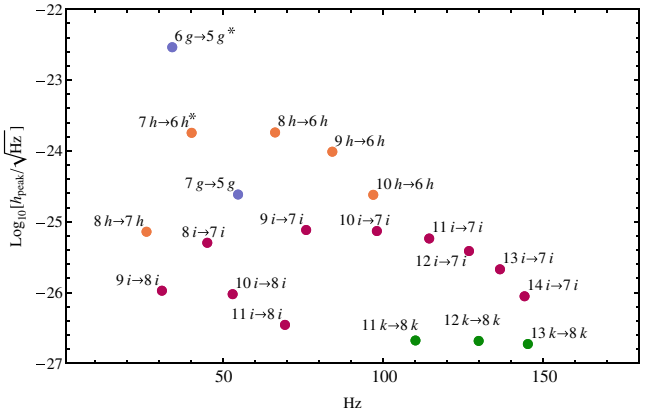

FIG. 4 (color online). Transition signal strains for different level transitions from a $10M_\odot$ black hole system 10 kpc away ($a_* = 0.99$, $\alpha/\ell = 0.3$), assuming 25 hr integration time. The bottom axis shows the corresponding GW frequency. We focus on the starred (*) transitions as most promising for GW detection. The strain shown here is approximate; we also make the simplistic assumption that in each case only two SR rates dominate.

If $\Gamma_g^{sr} > \Gamma_e^{sr}$ (Fig. 3, right), the excited level depopulates very quickly once it reaches the maximum, so the transition term for the ground state is never important. The smaller occupation number of the excited level suppresses the overall GW strain: the peak transition strain is smaller compared to the previous case by an additional factor of $\sqrt{\Gamma_e^{sr}/\Gamma_t}^{|\Gamma_e^{sr}-\Gamma_g^{sr}|/\Gamma_g^{sr}} \sim \mathcal{O}(10^{-35})^{|\Gamma_e^{sr}-\Gamma_g^{sr}|/\Gamma_g^{sr}}$.

In both cases, the transition process has a characteristic time scale of $\Gamma_{e,g}^{sr-1}$, typically decades for stellar BHs. The maximal occupation numbers are controlled by the ratio Γ_e^{sr}/Γ_t, and the peak strain is proportional to the superradiance rate:

$$h_{peak} \propto \frac{\Gamma_e^{sr}}{\sqrt{\omega_{tr}\Gamma_t}}. \quad (19)$$

The maximum signal occurs before the occupation numbers reach N_{max}; the ground state will continue to grow exponentially until all available angular momentum is extracted and the SR condition is no longer satisfied. At this point, annihilations become the dominant process. For general light bosons, the transition signal strain is unaffected as long as $N_{e,g}^{peak} < N_{bosenova}$, or $f_a \gtrsim 10^{14}$ GeV.

We assume above that the initial number of axions occupying each level is $N_{e0} = N_{g0} = 1$, as expected when superradiance starts from scratch. If it restarts after being disturbed e.g. by a bosenova which leaves one level partially occupied, the other level does not have time to grow to the optimal occupation number and the transition rate is not significant. This implies that the transition signal will most likely appear only once in the lifetime of a stellar black hole.

Figure 4 shows the relative GW strains of various transitions for a BH of mass $10M_\odot$. The analysis above shows that transitions are relevant for the evolution of superradiance only when the two levels can be simultaneously populated. The most promising cases for transition signals are the ones with the smallest difference between superradiance rates: $\Delta n \neq 0$ and $\Delta\ell = \Delta m = 0$. The $\ell = 4$ ("g") levels are ones with lowest ℓ that satisfy $\Gamma_e^{sr} > \Gamma_g^{sr}$ to avoid the suppression factor discussed above; levels with higher ℓ have lower superradiance rates and correspondingly lower peak strains. When three or more levels have similar superradiance rates, the transitions between them may be inhibited; such situations require further analysis. For instance, the $7h \to 6h$ transition suppresses the $8h \to 6h$ transition power (suppression not shown in Fig. 4).

We see that the $6g \to 5g$ transition is the most likely to be seen by GW detectors, followed by $7h \to 6h$; these are the levels that we use in our signal estimates below.

1. Advanced LIGO/VIRGO prospects

Transitions between superradiant levels around stellar black holes fall in the sensitivity band of Advanced LIGO and VIRGO: they have frequency $f \sim 15\,\mathrm{Hz} \times (\mu_a/10^{-11}\,\mathrm{eV})$ and peak strains as high as $h \sim 10^{-24}$ for a BH 10 kpc away. A search for such a signal with GW observatories is very promising, especially since the GW emission is monochromatic. The length of the signal for most of the observable parameter space is 10 years or more, so if a signal is detectable on Earth, it will persist longer than an observatory's science run.

The optimal search strategy is similar to an existing search for periodic gravitational waves from e.g. asymmetric neutron stars [21]. We base our estimates on the design aLIGO noise level [19]; we expect similar reach for Advanced VIRGO. The signal from a BH with $a_* = 0.99$ is visible up to 10 Mpc away, and one with $a_* = 0.9$ up to 30 kpc away; transition signal scales with the superradiance rate, so a black hole with larger spin can be seen from further away. The best reach is for masses around 3×10^{-11} eV (see Fig. 13 in Appendix B).

Given the promising reach, we can estimate the number of events aLIGO could observe, shown in Fig. 5. To quantify the event rate, we consider the probability to find a BH with high spin and mass in the appropriate range to lead to transitions, as well as the number and spatial distributions of BHs in our neighborhood young enough to be undergoing transitions today.

We use optimistic, realistic, and pessimistic estimates for the astrophysical distributions following the event rate estimates of the LIGO collaboration [22]. We fold the following astrophysical distributions of stellar BHs into our transition event rate estimates at aLIGO (see Appendix C for details):

(i) *Mass distribution*.—We use a fit to data with a minimum BH mass and exponential drop toward high masses characterized by $M_0 = 4.7^{+3.2}_{-1.9} M_\odot$ [23]. In Fig. 5 we use a minimum mass of $4.1 M_\odot$; the events shift to higher axion masses if the minimum BH mass is smaller. We show the central and 1σ widths of the mass distribution in Fig. 5.

(ii) *Spin distribution*.—We take the measured distribution, 30% of $a_* > 0.8$, as a realistic estimate for natal spins. We consider 90% above 0.9 optimistic and a flat distribution pessimistic.

(iii) *Formation rate*.—Barring rare violent events, the maximal transition signal occurs once per stellar BH lifetime, and the event rate is directly proportional to the BH formation rate. We estimate the BH birth rate to be $0.38^{+0.52}_{-0.3}$ per century based on supernova rates [24,25] and BH fraction of supernova remnants [26].

(iv) *Distance distribution*.—We assume the spatial distribution of BHs is proportional to the stellar distribution inside [27] and outside [28] the Milky Way. The event rates are dominated by black holes near the galactic center.

We can use the event rates to constrain a combination of the axion mass and astrophysical parameters. We isolate the most relevant astrophysical uncertainties, the BH formation rate and the spin distribution, and define

$$\epsilon \equiv \left(\text{BH formation rate}\right) \times \begin{pmatrix}\text{fraction of BHs} \\ \text{with} \quad a_* > 0.9\end{pmatrix}. \tag{20}$$

The 90% exclusion in the μ_a vs ϵ plane is shown in Fig. 6, fixing the BH mass and distance distribution to the central values discussed above. LIGO is not yet sensitive to reasonable astrophysical values for ϵ, but aLIGO will make considerable progress toward probing interesting parameter space.

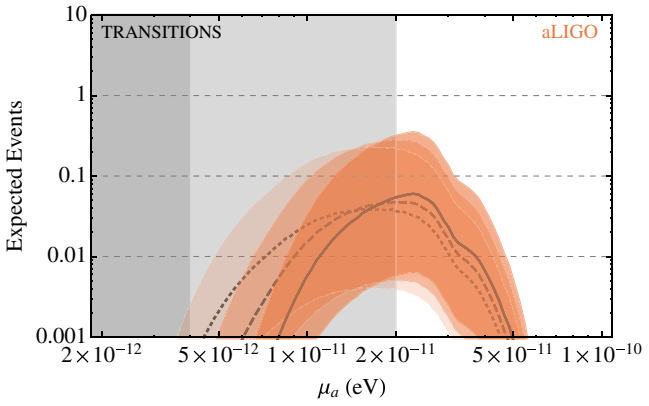

FIG. 5 (color online). Number of $6g \to 5g$ and $7h \to 6h$ transition events expected at aLIGO as a function of the axion mass, assuming a monochromatic search with 121×250 hr integration time and $C_{\rm tf} = 10$. Each event typically lasts several decades. We assume $4.1 M_\odot$ minimum BH mass; if the minimum BH mass is smaller the curves would shift to higher axion masses. The three lines correspond to varying the BH mass distribution width, from narrow (solid) to wide (dotted). The bands around the central curves correspond to optimistic and pessimistic estimates of other astrophysical uncertainties (see text). The vertical shaded regions are disfavored by the observation of rapidly spinning BHs, for bosons with coupling equal to that of the QCD axion (light gray) or stronger (dark gray) (see Sec. IV).

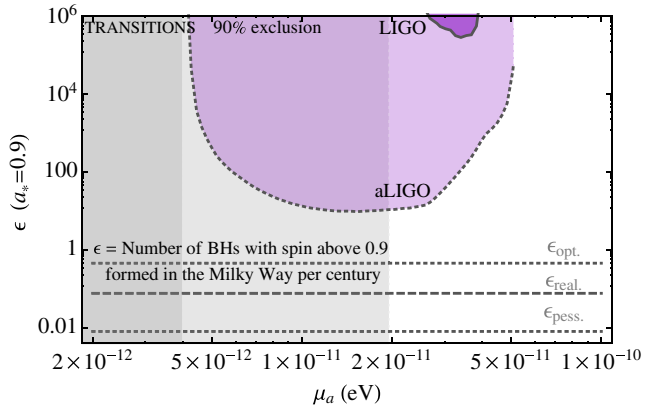

FIG. 6 (color online). LIGO and projected aLIGO exclusion for $6g \to 5g$ and $7h \to 6h$ transitions. The vertical shaded regions are the same as in Fig. 5. We assume BH mass and distance distribution as described in the text. For the LIGO curve, we use the same integration time as the current LIGO monochromatic search, $N_{\rm seg} = 121$, $T_{\rm coh} = 25$ hrs, and $C_{\rm tf} = 20$; for aLIGO, we use $N_{\rm seg} = 121$, $T_{\rm coh} = 250$ hrs, and $C_{\rm tf} = 10$. The horizontal lines indicate optimistic, realistic, and pessimistic values for the ϵ-parameter.

Unlike the case of neutron stars which spin down due to GW emission, the transition signal's frequency is set by the level splitting and is constant up to corrections from the nonlinearities of the cloud itself. For the QCD axion, the maximum signal occurs when the occupation number of the cloud is much smaller than the nonlinear regime, resulting in a tiny frequency drift,

$$\frac{df}{dt} \simeq 10^{-11}\ \frac{\mathrm{Hz}}{\mathrm{s}} \left(\frac{f}{90\ \mathrm{Hz}}\right) \left(\frac{M}{10 M_\odot}\right) \left(\frac{10^{17}\ \mathrm{GeV}}{f_a}\right)^2 \left(\frac{5\ \mathrm{yr}}{T}\right)^2, \tag{21}$$

where $T \gtrsim 5$ yr is the characteristic signal length, set by $\Gamma_{\mathrm{sr}}^{-1}$; most of our parameter space has smaller frequency drift, down to 10^{-20} Hz/s, and the signal is well approximated as having a constant frequency.

While the change in frequency is small, observing and correlating it with the signal amplitude can provide additional handles on the magnitude and sign of the particle's self-interaction. The amplitude and sign of the frequency drift are correlated with the amplitude of the signal. If $\Gamma_g^{\mathrm{sr}} > \Gamma_e^{\mathrm{sr}}$, the frequency of the emitted graviton increases with time. If $\Gamma_g^{\mathrm{sr}} < \Gamma_e^{\mathrm{sr}}$, the frequency decreases as both levels grow and then increases as the excited level empties. For particles with repulsive interactions, the drift is in the opposite direction.

The theoretical uncertainties of the expected event rates and exclusions depend on the SR rate and the transition rate, the precise values of which require further numerical study to include higher order effects of the metric and deviations from the hydrogen wave functions which we assume in our estimates. The dependence on the SR rate is mild since a larger SR rate leads to larger signal strain but shorter signal length. The dependence on the transition rate is stronger; event rates and exclusions scale with $\sim\Gamma_t^{-1/2}$, which we expect to have uncertainties of $\mathcal{O}(1)$.

If there is an axion or light boson close to 10^{-11} eV in mass, with some luck, aLIGO could see a monochromatic signal lasting for many years.

2. Future gravitational wave observatories

Upcoming observatories such as Advanced LIGO and VIRGO are perfectly suited to search for superradiance signals from stellar black holes; to detect SR signals from supermassive black holes (SMBHs), we look to future, lower-frequency proposals: eLISA and AGIS. The eLISA observatory is a laser interferometry gravitation wave detector [29]; LISA Pathfinder is planned to test milestone requirements in its experimental development [30]. AGIS is a recently proposed single-baseline gravitational wave detector based on atom interferometry [31]. This promising new idea is currently under development and could exceed light-based interferometer sensitivities [32,33].

The reach of eLISA and AGIS is promising, extending to as far as a hundred Mpc, but the best detector sensitivity falls in the range of intermediate-mass black holes (BHs), $M \lesssim 10^5 M_\odot$ (see Fig. 14 in Appendix B). Lack of estimates for distributions of intermediate mass BHs makes even an approximate estimate of event rates difficult. In the limit where all supermassive black holes have mass $M = 10^6 M_\odot$ and most have maximal spin (see Appendix C), low-frequency detectors can observe up to 100 BHs undergoing transitions.

B. Annihilations

Another source of gravitational wave emission is axions annihilating to gravitons in the black hole background, $a + a \to g + g_{\mathrm{bg}}$; this process is analogous to electron-positron annihilation to a photon in the background of a nucleus [34]. The GW frequency is

$$\omega_{\mathrm{ann}} = 2\omega_a \simeq 2\mu_a \left(1 - \frac{\alpha^2}{2n^2}\right). \tag{22}$$

When a single level dominates the evolution of the axion-BH system, its occupation number $N(t)$ grows with its SR rate while being depleted by axions pair annihilating into gravitons,

$$\frac{dN}{dt} = \Gamma_{\mathrm{sr}} N - \Gamma_a N^2. \tag{23}$$

Here, Γ_a is the annihilation rate for one pair of axions, of order

$$\Gamma_a \simeq 10^{-10} \left[\left(\frac{\alpha/\ell}{0.5}\right)^p + \mathcal{O}\left(\frac{\alpha/\ell}{0.5}\right)^{p+1}\right] \frac{G_N}{r_g^3}, \tag{24}$$

where $p = 17$ for $\ell = 1$ and $p = 4\ell + 11$ for $\ell \geq 2$; see Appendix A for full expressions and a discussion of the α dependence of the $\ell = 1$ level. We only consider $n = \ell + 1$ in this section. The annihilation rates close to the superradiance boundary ($\alpha/\ell = 1/2$) are similar for all ℓ-levels. At smaller α/ℓ, the annihilation rate is velocity suppressed, with the suppression more pronounced at higher ℓ.

Comparing Eqs. (16) and (24) we see that annihilation is the slowest process, $\Gamma_a \ll \Gamma_t \lll \Gamma_{\mathrm{sr}}$. Nevertheless, annihilations are important when the occupation number of a single level is far larger than that of the others, as is the case when a single superradiance rate dominates.

When $N < \Gamma_{\mathrm{sr}}/\Gamma_a$, the axion population grows exponentially with the superradiance rate. Once the axion cloud extracts the maximum possible spin from the BH, $N(t) = N_{\mathrm{max}}$, superradiance shuts off and the occupation number evolves as

$$N(t) = \frac{N_{\max}}{1 + \Gamma_a N_{\max} t}. \quad (25)$$

The corresponding gravitational wave signal strain is

$$h(t) = N(t)\sqrt{\frac{4G_N}{r^2 \omega_{\rm ann}}\Gamma_a}. \quad (26)$$

Both the peak strain,

$$h_{\rm peak} \simeq 10^{-22}\left(\frac{1\ {\rm kpc}}{r}\right)\left(\frac{\alpha/\ell}{0.5}\right)^{\frac{p}{2}}\frac{\alpha^{-\frac{1}{2}}}{\ell}\left(\frac{M}{10M_\odot}\right), \quad (27)$$

and peak duration, $(N_{\max}\Gamma_a)^{-1}$, are independent of the superradiance rate. For stellar BHs, the signal at its peak value can last for thousands of years.

For supermassive black holes, we expect the BH to move adiabatically on the Regge trajectory since $(N_{\max}\Gamma_a)^{-1}$ is of order 10^9 years, comparable to the Eddington accretion time. The motion of the BH along the Regge trajectory may be interrupted by infalling stellar mass BHs or neutron stars; we estimate that such events occur every 10^6–10^7 years based on the star infall rate in [35] and that about one in 100 stars is a BH or neutron star [36]. When this happens, $\mathcal{O}(1)$ of the cloud falls back into the black hole, restoring the spin almost back to the value that it would have had without superradiance. We require that the superradiance rate is much larger than the violent infall event rate; then except for short intervals around the time of the infall, the signal coming from annihilations will be close to maximal until the black hole grows in mass such that it is no longer affected by superradiance. While the infall rate is uncertain, it only affects a small part of the parameter space. The size of the cloud is determined by the difference between the spin the BH would have had without superradiance and the spin corresponding to its mass on the trajectory. Figure 9 takes into account these subtleties for supermassive black holes.

So far, we have assumed that the axion's self-interaction is of QCD axion strength. If the interaction is stronger such that bosenovae are relevant, the axion cloud only grows to $N_{\rm bosenova} < N_{\max}$, and the maximum annihilation signal is proportionally smaller and lasts for a shorter time.

1. Advanced LIGO/VIRGO prospects

The annihilation signal is quite distinctive: it is monochromatic with frequency of twice the axion mass, $f = 10\ {\rm kHz} \times (\mu_a/10^{-11}\ {\rm eV})$, possibly lasting for thousands of years. The optimal reach of aLIGO is for axion masses around 5×10^{-13} eV which correspond to intermediate mass black holes, $M > 30M_\odot$ (see Fig. 15 in Appendix B); these are poorly understood and have only been recently observed [37].

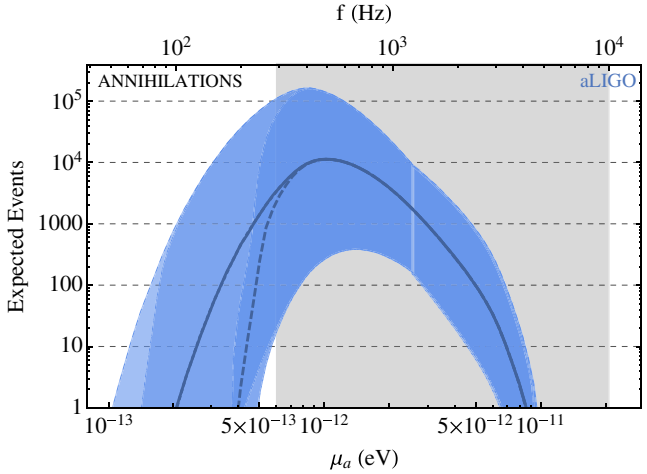

FIG. 7 (color online). Number of $2p$ annihilation events possible to observe with aLIGO as a function of the axion mass, assuming a monochromatic search with 121×250 hr integration time and $C_{\rm tf} = 10$. Each event lasts thousands of years or longer. The vertical shaded region is disfavored by black hole spin measurements assuming QCD axion coupling strength. Each of the three bands corresponds to cutting off the BH mass distribution at a maximum mass of $\{30, 80, 160\}M_\odot$ (dark, medium, and light blue) including optimistic and pessimistic estimates of astrophysical uncertainties, with central values given by the dashed ($M_{\max} = 30M_\odot$) and solid ($M_{\max} = 80, 160M_\odot$) curves (see text).

To estimate the event rate, we use the mass distribution of stellar BHs, which includes an exponential tail extending to heavier BHs. In Fig. 7, we estimate the event rate expected in aLIGO from axion annihilations using the same BH astrophysical distributions as in Sec. III A 1. We folded the BH mass distribution width into the optimistic and pessimistic estimates, and we indicate the expected event rate for different maximum stellar BH mass cutoffs (see Appendix C). Especially at light axion masses, the signal is subject to large astrophysical uncertainties of heavier (30–100$M_\odot$) BH mass distributions, and the difference between the optimistic and pessimistic estimate is dominated by the shape of the exponential tail of the BH mass distribution.

The event rates range from $\mathcal{O}(1)$ to $\mathcal{O}(10^4)$; part of the parameter space with appreciable event rates is disfavored by BH spin measurements (Sec. IV). The event rates for axion masses lighter than the excluded range are very promising, with possibly thousands of monochromatic signals due to a Planck-scale QCD axion or another boson in the same mass range.

Similarly to our exclusion in Fig. 6 for transition signals, we place an exclusion in the ϵ [Eq. (20)] vs axion mass plane in Fig. 8, fixing the distance distribution as discussed above and using a conservative mass distribution with a narrow width and upper BH mass cutoff of $80M_\odot$. The reach for annihilations covers much of the region

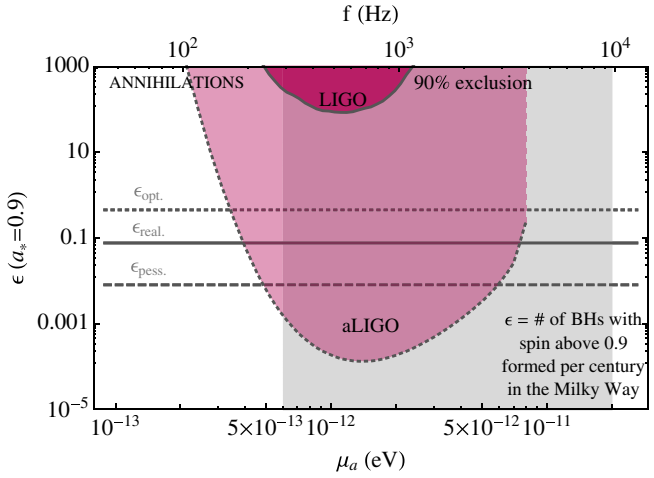

FIG. 8 (color online). LIGO and projected aLIGO exclusion for $2p$ annihilations. The vertical shaded region is the same as in Fig. 7. We assume BH mass and distance distribution as described in the text. For the LIGO curve, we use the same integration time as the current LIGO monochromatic search, $N_{\rm seg} = 121$, $T_{\rm coh} = 25$ hrs, and $C_{\rm tf} = 20$; for aLIGO, we use $N_{\rm seg} = 121$, $T_{\rm coh} = 250$ hrs, and $C_{\rm tf} = 10$. The horizontal lines indicate optimistic, realistic, and pessimistic values for the ϵ-parameter.

disfavored by black hole spin measurements and can provide a cross-check for the exclusion. The large event rates make detection in the mass range of $1\text{–}6 \times 10^{-13}$ eV possible, and aLIGO can probe a meaningful region in the axion parameter space.

Advanced LIGO is sensitive largely to signals from within the Milky Way. An increase in detector sensitivity by a factor of 10 (such as the Einstein Telescope [21]) would increase the number of events by a factor of $\mathcal{O}(10)$: the detector would be sensitive to signals with smaller strain which last for a proportionally longer time. To reach a cubic scaling with distance the detector reach must be >30 Mpc, at which point the density of galaxies scales in proportion to the volume. This would require a detector with sensitivity a factor of 100 better than aLIGO.

The theoretical uncertainties in the expected annihilation event rates are independent of the superradiance rate, while an $\mathcal{O}(10)$ increase in the annihilation rate extends the reach to lower μ_a by ∼20%. The change is not significant because a higher signal strain is compensated by a shorter signal length. As explained in Appendix A, we expect the $2p$ annihilation rate to have a weaker α-dependence than our conservative analytical estimate. Changing the α-dependence would extend the event and exclusion curves by a factor of ∼2 toward lighter μ_a and increase the peak event rates by a factor of ∼4.

Large frequency drift can make a monochromatic search difficult. In the case of annihilations, the signal grows to a maximum with the superradiance rate, and the cloud then slowly depletes, resulting in a small positive drift in frequency due to attractive self-interactions,

$$\frac{df}{dt} \simeq 10^{-12}\ \frac{\rm Hz}{\rm s}\left(\frac{f}{\rm kHz}\right)\left(\frac{M_{\rm Pl}}{f_a}\right)^2\left(\frac{10^3\ \rm yr}{T}\right), \qquad (28)$$

where $T = (\Gamma_a N_{\rm max})^{-1}$ is the typical length of the signal. For most of the parameter space, the frequency drift is smaller than 10^{-12} Hz/s. In our exclusion estimate above, we only include signals that have frequency drift smaller than 7×10^{-11} Hz/s (7×10^{-13} Hz/s) for coherent integration time of 25 (250) hrs based on the frequency binning in [21]. If the experimental search techniques can accommodate higher frequency drift, aLIGO can be sensitive to $\mathcal{O}(10\%)$ higher axion masses.

If a frequency drift is detected, it can be used to distinguish the signal from astrophysical sources. With the large number of events expected, an additional tool to distinguish signal from astrophysical sources is the detection of multiple monochromatic lines with frequencies $\sim 2\mu_a$, differing by corrections from the $\mathcal{O}(\alpha^2)$ binding energy to the BH [Eq. (22)].

The astrophysical uncertainties are large, but the event rates are very promising. If a signal is identified, further study of its amplitude and frequency as a function of time, correlated with astrophysical measurements of the black hole source, could determine the mass and coupling of the superradiating particle.

2. Future gravitational wave observatories

The frequency sensitivities of AGIS and eLISA are ideal for detection of axion annihilations around supermassive black holes, with a promising reach of up to 300 Mpc in distance for axions between 10^{-18}–10^{-17} eV (see Fig. 16 in Appendix B).

The masses and spins of supermassive black holes are determined by long periods of accretion and so possible to estimate theoretically. We use the following distributions for the event rates (more details in Appendix C):

(i) *Mass and distance distribution*.—We use the distributions of [38,39], with most SMBHs between 10^6 and $10^7 M_\odot$ in mass and about one $10^7 M_\odot$ BH per Milky-Way type galaxy.

(ii) *Spin distribution*.—The biggest uncertainty for event rates is due to the unknown spin distribution of SMBHs. We use a range of model predictions: optimistic, 70% of SMBHs have spins $a_* \geq 0.93$ [40]; intermediate, 70% have spins $a_* \geq 0.7$ with 50% above 0.9 [41]; and pessimistic or low spin $a_* = 0.2 \pm 0.2$ [42]. The event rates are dominated by SMBHs with spins above 0.9.[3]

(iii) *Signal length*.—Most of the evolution of a SMBH which satisfies the SR condition is at the regime

[3]We thank an anonymous referee for proposing the above benchmarks for spin distributions and pointing us to the relevant references. See Appendix C for further details.

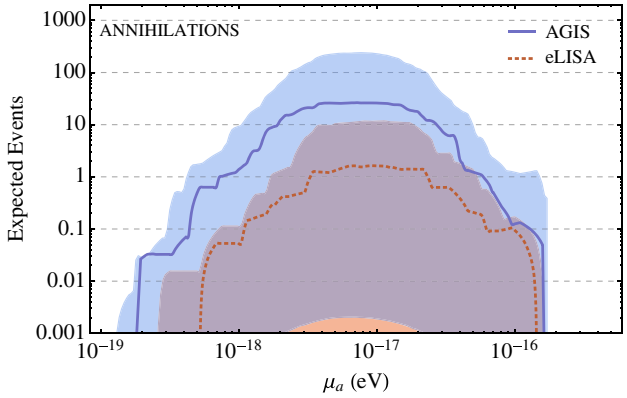

FIG. 9 (color online). Expected number of events in eLISA (dashed) and AGIS (solid) as a function of the axion mass for SMBHs with axions in the $2p$-level undergoing annihilations. Each event can last millions of years. The shaded bands bracket the optimistic and pessimistic estimates, dominated by SMBH spin distributions (see text).

where accretion, superradiance, and axion annihilation happen adiabatically. This agrees with numerical results in [43]. In this case BH spin and axion cloud size remain in a steady state with annihilations at the maximum rate.

We estimate the event rate expected by AGIS and eLISA in Fig. 9, giving the realistic as well as the optimistic and pessimistic estimates based on the astrophysical uncertainties above. The differences in sensitivity of the two detectors are of order the astrophysical uncertainties. If there is a light boson with mass of 10^{-18}–10^{-16} eV, the annihilation signal is dramatic, with thousands of continuous events visible.

C. Bosenovae

A very different signature is the periodic collapse of the axion cloud, known as a bosenova in analogous condensed matter systems. If the axion self-interaction is sufficiently strong ($f_a \ll M_{\rm pl}$), the axion cloud will collapse at the critical size $N_{\rm bosenova}$ before extracting all the BH's spin as allowed by the superradiance condition. During the bosenova, a fraction of the cloud falls into the black hole and the rest escapes to infinity, emitting a gravitational wave burst.

The collapse lasts for approximately an infall time, $t_{\rm bn} = (c_{\rm bn} r_c)$, and has primary frequency component

$$f_{\rm bn} \sim 30\ {\rm Hz} \left(\frac{16}{c_{\rm bn}}\right) \left(\frac{\alpha/\ell}{0.4}\right)^2 \left(\frac{10 M_\odot}{M}\right), \qquad (29)$$

where $c_{\rm bn}$ parametrizes the collapse time ($c_{\rm bn} \sim 16$ for the $2p$ level [17]).

Once the size of the cloud is reduced such that the system is no longer nonlinear, the level grows again with its superradiance rate until the next bosenova, and the growth-collapse cycle repeats until the superradiance condition is no longer satisfied. The separation between bursts depends on the fraction of the cloud which remains bound to the BH after the bosenova event.

For example, the collapse of a typical axion cloud around a $10M_\odot$ black hole with spin $a_* = 0.99$ will emit a burst lasting 10^{-3} s. If the axion coupling is e.g. $f_a = 6 \times 10^{16}$ GeV, and each bosenova depletes the cloud to a size of $10^{-4} N_{\rm bosenova}$, the signal will be in the distinct pattern of ten spikes separated by quiet periods of 300 s.

The strain of these periodic bursts can be large enough to be observed by aLIGO: at a distance of a kpc, the quadrupole estimate gives a signal strain of

$$h \simeq 10^{-21} \left(\frac{\sqrt{\epsilon}/c_{\rm bn}}{10^{-2}}\right)^2 \left(\frac{\alpha/\ell}{0.4}\right) \left(\frac{M}{10 M_\odot}\right) \left(\frac{f_a}{f_a^{\rm max}}\right)^2, \qquad (30)$$

where ϵ is the fraction of the cloud falling into the BH ([17] gives $\epsilon \sim 5\%$) and $f_a^{\rm max}$ is the largest f_a for which bosenovae occur, Eq. (10). For a $10M_\odot$ BH, $f_a^{\rm max}$ corresponds to a small quartic coupling of $\lambda \sim 10^{-77}$ for a generic scalar boson.

As we saw earlier, the QCD axion coupling is most likely too weak to cause bosenovae around astrophysical black holes; light bosons with larger self-couplings can lead to bosenovae that occur with a tell-tale regularity and with signal frequency and strain that fall promisingly in the range of aLIGO. Calculation of detector reach and event rates are beyond the scope of this paper; dedicated numerical study is necessary to determine the precise shape, timing, and amplitude of the bosenovae emission.

IV. BOUNDS FROM BLACK HOLE SPIN MEASUREMENTS

Several techniques for spin measurements of black holes have been developed and are constantly improving. The leading methods are continuum fitting and x-ray relativistic reflection (for recent reviews, see [44] and [45]). Both are based on the measurement of the innermost stable circular orbit of the accretion disk: the radius ($R_{\rm ISCO}$) at which matter in the disk stops smoothly orbiting and rapidly falls into the black hole. The $R_{\rm ISCO}$ is a monotonically decreasing function of a_* that becomes steeper for $a_* \sim 1$, reducing error on high-spin measurements [46]. The systematics for converting $R_{\rm ISCO}$ to a spin measurement are the same for both methods, but the systematics for measuring $R_{\rm ISCO}$ are distinct.

Continuum fitting measures the $R_{\rm ISCO}$ through the temperature and luminosity of the accretion disk. As the innermost stable circular orbit gets closer to the BH horizon, the matter becomes denser and hotter, increasing the luminosity of emitted radiation. The luminosity does not depend in detail on the disk model: as matter orbits toward the BH, its gravitational potential energy is converted to orbital kinetic energy, with the amount radiated

away determined only by assumptions of steady state rotation, axisymmetry, and conservation laws [44]. Just like the measurement of a star's radius from its temperature and luminosity, the $R_{\rm ISCO}$ measurement relies on the absolute distance to the BH and the disk inclination with respect to line of sight. These, along with the BH mass needed to convert $R_{\rm ISCO}$ to the dimensionless quantity a_*, lead to the dominant sources of error in the spin measurement [44,47,48]. Subleading uncertainties from disk modeling result in less than 10% error in $R_{\rm ISCO}$ and $<3\%$ errors in a_* at high spins. The limitation is that the peak emission must be clearly visible, excluding SMBHs for which emission is in the unobserved far-UV or soft x-ray frequencies.

The x-ray relativistic reflection method (also known as Fe-K or broad iron line method) measures the properties of the Fe-Kα spectral line, which is excited in the accretion disk by an external x-ray source (e.g. the disk corona or the base of a jet); it can be used to measure spins of both supermassive and stellar BHs. The x rays are partially absorbed, leading to an emission line from deexcitation with a particularly distinctive shape. Little emission occurs inside $R_{\rm ISCO}$ since there the density of matter drops sharply. For higher spin, matter can be closer to the horizon, resulting in an iron line with a longer gravitationally redshifted tail [49]. If the disk is tilted, the rotation of the disk Doppler shifts the line to the blue and the red, resulting in two peaks. Since iron has high abundance and high fluorescence, and is isolated in the spectrum, the broadened and distorted line can be fitted to find $R_{\rm ISCO}/r_g$ and the inclination of the disk [50]. The Doppler and gravitational shifts both depend on the dimensionless quantity $R_{\rm ISCO}/r_g$, so knowledge of the BH mass is not needed to find a_*.

A. Spin limits

Dozens of stellar and supermassive black hole spins have been measured to date with the techniques described above. Since a black hole that satisfies the superradiance condition loses its spin quickly on astrophysical time scales, these measurements place limits on previously unexplored light boson parameter space.

In Fig. 10 we show example regions in the BH spin-mass plane affected by the superradiance of a QCD axion with $\mu_a = 10^{-11}$ eV. The shaded areas correspond to the $\ell = 1, \ldots 5$ levels that satisfy the SR condition, separated by Regge trajectories. A black hole excludes the axion mass if the SR condition is satisfied for at least one ℓ-level and, within experimental error, the corresponding superradiance rate is fast enough to grow a maximally filled cloud, $\Gamma_{\rm sr}\tau_{\rm bh} \geq \log N_{\rm max}$. The relevant time scale $\tau_{\rm bh}$ is the shortest on which SR can be disturbed: for stellar BHs, we use the shorter of the age and the Eddington accretion time; for SMBHs, we use the compact-object infall time ($\tau_{\rm bh}$ varies between systems so the regions shown in Fig. 10 are approximate).

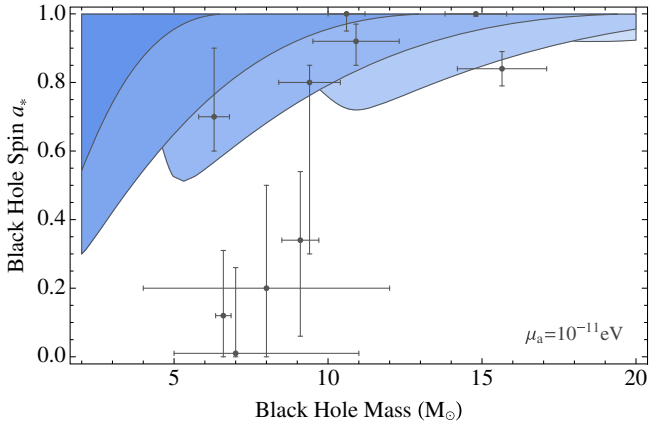

FIG. 10 (color online). The shaded regions are affected by superradiance and bounded by Regge trajectories in the presence of a QCD axion with mass $\mu_a = 10^{-11}$ eV. The points are stellar black hole measurements with 1σ error bars (for the two fastest spinning BHs, the 2σ lower spin bounds are shown).

Figure 10 also includes BH spin and mass data with 1σ error bars, except for the lower spin limit for the two highest spin BHs, which are quoted at 2σ. The QCD axion mass and coupling as pictured are clearly excluded by the two fastest-spinning BHs. Increasing the mass of the axion shifts the affected regions to the left, relaxing the bound. Increasing the axion self-coupling relaxes the limits as well: instead of growing to maximum size all at once, each time the cloud reaches the critical size $N_{\rm bosenova}$ it collapses, so the SR rate has to be larger to extract the spin in the same period, $\Gamma_{\rm sr}\tau_{\rm bh}(N_{\rm bosenova}/N_{\rm max}) \geq \log N_{\rm bosenova}$. In addition, the BH can be trapped on the Regge trajectories; if the spin and mass of a black hole indicate that it may be on a Regge trajectory, we only use it to place bounds if it stays there for a short time, $\tau_{\rm regge} \ll \tau_{\rm bh}$.

We show the resulting bounds in Fig. 11. Each black hole places a limit on a range of axion masses and each ℓ-level leads to the distinct lobes of the exclusion region; higher levels have longer superradiance times and give increasingly weaker constraints. For large axion masses, there is no measured BH light enough to satisfy the SR condition; for axion masses too small, the "atomic coupling" α is too weak, resulting in a too-slow spin extraction rate or too-quick mode mixing (Sec. V) in the presence of perturbation from the BH companion star. For strong self-interactions ($N_{\rm bosenova} \ll N_{\rm max}$), the bounds no longer apply; this is in contrast with typical laboratory experimental limits for axions which are relaxed if interactions are sufficiently weak.

The bounds rely on our computation on the SR rate, and so have some theoretical uncertainty. On the right edge of the bound, a higher SR rate for high-ℓ levels would increase the exclusion while a faster drop of the rate near

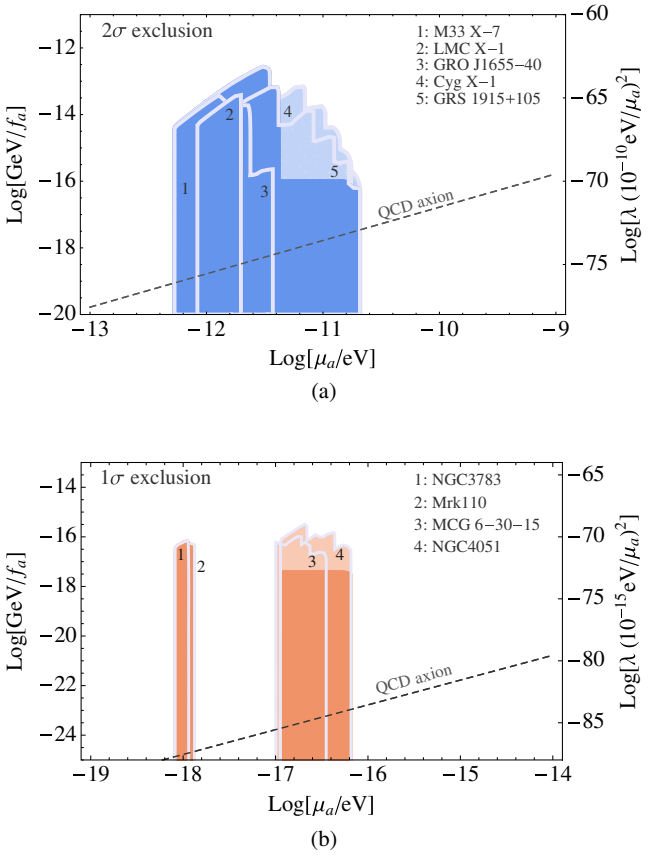

FIG. 11 (color online). Limits on mass and self-coupling of light axions derived from (a) quickly rotating stellar black holes (at 2σ) and (b) quickly rotating supermassive black holes (at 1σ). The limits disappear for lower f_a because the axion cloud can collapse due to self-interactions before extracting a significant fraction of the BH's spin. The lighter regions are where the BH may be on a Regge trajectory and are therefore not excluded. We also translate the f_a dependence to the quartic coupling λ (right axes).

the SR boundary would decrease it. The top of the exclusion varies as the square root of bosenova size, and logarithmically on the SR rate. At small α there is the possibility of mode mixing due to the companion star (Sec. V); the bound at light axion masses has a $\mathcal{O}(10\%)$ uncertainty assuming $\mathcal{O}(1)$ uncertainties in SR rates and deviations of the cloud profile in the Kerr metric from hydrogen wave functions.

We present more details about the stellar black holes we use to set limits in Table III. These have spins determined by both methods, as well as precise mass measurements and an estimated age for the BH system. Stellar BH limits are quite robust: the binary systems are well studied, as seen from the measurements of BH properties. These exclude the mass range $2\times10^{-11} > \mu_a > 6\times10^{-13}$ eV, corresponding to $3\times10^{17} < f_a < 1\times10^{19}$ GeV for the QCD axion: parameter space that has not been reached with any other approach so far (but see [51] for an experimental proposal to search for high-f_a axions).

Table IV lists the masses and spins of SMBHs we use to set limits. Their ages are unknown, but it is understood that they accrete to reach their current mass, so the age is by definition longer than the accretion time [39]. The dynamical time scale $\tau_{\rm bh}$ is instead set by violent events. Recent measurements indicate that a star falls into a given SMBH roughly every 3×10^4 years [35]. The star is incorporated into the accretion disk; however, an infalling BH or neutron star could cause a large perturbation to the cloud. To estimate the rate of such violent events, we conservatively take 10^{-2} of the star infall rate, since about one in 100 stars is a BH [36].

The properties of the SMBHs are less well-known, and the spin measurements so far employ only the x-ray method [50], so we consider our limits preliminary.

As more black holes are measured with higher precision, the limits may extend further. If, on the other hand, a light axion is nearby, the data will begin to trace out Regge trajectories where the BH is likely to remain for long times: in Fig. 10, we expect to find BHs only outside the SR regions or on their boundaries. This requires a lot of progress, but can be another avenue toward axion detection. Black holes that may be on Regge trajectories are also candidate point sources for directed GW searches, as they may be emitting GWs from annihilations.

TABLE III. Stellar black holes that set limits on light bosons (data compiled in [44] unless otherwise specified). Errors for masses are quoted at 1σ, spin limits at 2σ[a]. GRO J1655 − 40 has a 2σ-discrepancy between continuum fitting and x-ray reflection [45]; we use the continuum spin values, which are lower. GRS1915 + 105 has periods of unusually high luminosity: the spin measurement [52] uses only data from the low-luminosity periods, when $\dot{M}/\dot{M}_E < 0.3$; in addition, we conservatively use $\tau_{\rm bh} = \tau_{\rm eddington}/10$ to set the limit.

No.	Object	Mass ($M_\odot$)	Spin	Age (yrs)	Period (days)	$M_{\rm comp\ star}$ ($M_\odot$)	$\dot{M}/\dot{M}_E$
1	M33 X-7	15.65 ± 1.45	$0.84^{+0.10}_{-0.10}$ [53]	3×10^6 [54]	3.4530 [55]	$\gtrsim$20 [55]	$\gtrsim$0.1 [55]
2	LMC X-1	10.91 ± 1.4	$0.92^{+0.06}_{-0.18}$ [56]	5×10^6 [54]	3.9092 [57]	31.79 ± 3.48 [57]	0.16 [57]
3	GRO J1655 − 40	6.3 ± 0.5	$0.72^{+0.16}_{-0.24}$ [53]	3.4×10^8 [58]	2.622 [58]	2.3–4 [58]	$\lesssim$0.25 [59]
4	Cyg X-1	14.8 ± 1.0	>0.99 [60]	4.8×10^6 [61]	5.599829 [54]	17.8 [54]	0.02 [54]
5	GRS1915 + 105	10.1 ± 0.6	>0.95 [53,62]	4×10^9 [63]	33.85 [64]	0.47 ± 0.27 [64]	$\gtrsim$1 [64].

[a]We thank J. Steiner and J. McClintock for providing the latest 2σ errors on the spin measurements.

TABLE IV. Supermassive black holes with reliable mass and spin measurements (compiled in [45,50]) used to set limits on light bosons in Fig. 11(b). The mass errors are quoted at 1σ and the spin measurements at 90% confidence. While many more spin measurements are available, our analysis excludes BHs which do not have an error estimate on the mass.

No.	Object	Mass ($10^6 M_\odot$)	Spin
1	NGC 3783	29.8 ± 5.4	>0.88
2	Mrk 110	25.1 ± 6.1	>0.89
3	MCG-6-30-15	$2.9^{+0.18}_{-0.16}$	>0.98
4	NGC 4051	1.91 ± 0.78	>0.99

V. EFFECT OF THE BLACK HOLE ENVIRONMENT

So far, we have considered an isolated black-hole-axion system; in this section, we show that this is a good approximation. The companion star orbits far from the black hole and the accretion disk contains a small fraction of the black hole mass spread over a large region; we will see that the perturbation due to the environment is irrelevant for GW signal parameter space, although it can slightly affect the bound derived from high-spin BHs for very large clouds, $\alpha/\ell \ll 1$.

A nonuniform, asymmetric perturbation near the black hole can mix the superradiating and dumping (infalling) levels of the cloud and cause part of the axion cloud to collapse. We consider a static perturbing potential $\delta V(\vec{r})$: orbital frequencies of the companion star and accretion disk are much smaller than the axion energy, so the perturbation is adiabatic. The condition that at the horizon the energy flux is negative, i.e. more axions are extracted from the ergo-region than fall back in, is

$$\left|\frac{\Gamma^{n'\ell'm'}_{\rm dump}}{\Gamma^{n\ell m}_{\rm sr}}\right|^{1/2}\left|\frac{\langle\psi^{n'\ell'm'}_{\rm dump}|\delta V(\vec{r})|\psi^{n\ell m}_{\rm sr}\rangle}{\Delta E}\right| < 1, \qquad (31)$$

where $\psi_{\rm sr,dump}$ are the wave functions of the superradiating and dumping levels, ΔE is the energy difference between them, and $\Gamma_{\rm dump}$ and $\Gamma_{\rm sr}$ are the analytical dumping and superradiant rates [2] (an excellent approximation at small α/ℓ). The ratio of the rates comes from relating the wave functions at the cloud to those at the horizon [4] and scales as a high power of α,

$$\Gamma^{n'\ell'm'}_{\rm dump}/\Gamma^{n\ell m}_{\rm sr} \propto \alpha^{4(\ell'-\ell)} \quad (\alpha/\ell \ll 1), \qquad (32)$$

with a weaker dependence on m.

The energy differences ΔE are $\mu_a(\alpha/n)^2$ between levels with $\Delta n \neq 0$, with $\sim\mu_a(\alpha/\ell)^4$ "fine" level splitting from relativistic corrections (if $\Delta\ell \neq 0$) and $\sim\mu_a(\alpha/\ell)^5$ "hyperfine" splitting from spin-orbit coupling (if $\Delta m \neq 0$),

$$\Delta H_{\rm s.o.} = \boldsymbol{\mu}_{\rm axion\text{-}orbit}\cdot\boldsymbol{B}_{\rm bh} \sim \frac{a_*}{r_g}\left(\frac{\alpha}{\ell}\right)^6, \qquad (33)$$

and higher order corrections to the Newtonian potential from the black hole.

A. Companion star

The observed stellar BHs are in binaries with companion stars, the masses and especially orbital periods of which are known to great precision (Table III). For the systems used in setting limits, the companions have mass M_* of order the BH mass and orbit at a distance $R \sim 10^6 r_g$ from the BH. To compute the effect of the companion, we decompose its gravitational potential into multipoles; schematically,

$$\frac{\delta V}{\mu_a} \sim \frac{M_*}{M}\frac{r_g}{R}\left(1 + \frac{r_c}{R}Y_{1,m} + \frac{r_c^2}{R^2}Y_{2,m} + \cdots\right). \qquad (34)$$

The leading contribution comes from the dipole ($\ell' = \ell - 1$) term of order $r_c^2/R^2 \ll 1$; the resulting mixing does not affect superradiant growth if

$$\left(\frac{\alpha}{\ell}\right) \gtrsim (0.05)\left(\frac{M_*}{10M_\odot}\right)^{\frac{1}{8}}\left(\frac{M}{10M_\odot}\right)^{\frac{1}{24}}\left(\frac{\rm day}{T}\right)^{\frac{1}{6}}, \qquad (35)$$

where T is the orbital period of the companion star and M is the black hole mass. Higher multipoles mix with other $\ell' \neq \ell$ modes and give a comparable bound, while mixing with $\Delta\ell = 0, m' \neq m$ modes gives a weaker bound since the ratio of dumping to superradiance rates for these modes is smaller. Thus, a typical companion star may disrupt superradiance only if the axion–black hole coupling is small, $\alpha/\ell < 0.05$; the bound has very weak dependence on the black hole binary parameters. We take this constraint into account in setting limits on axion parameter space. For our GW signal estimates, the bound on α/ℓ is irrelevant: the weak coupling produces signals too small to observe, and signals are just as likely to come from the over 50% of BHs which are not in binaries [65].

B. Accretion disk

Stellar BHs in binaries and supermassive BHs are surrounded by accretion disks which extend out from the innermost stable orbit. For stellar black holes, the accretion disk extends to the companion star at $10^6 r_g$, while for a $M = 10^8 M_\odot$ black hole, the disk ends at $\sim 10^3 r_g$ [66]. Although the disk can spatially overlap with the axion cloud, it does not source a large perturbing potential since the mass in the disk is very small compared to the BH mass. To compute the effect on the axion cloud, we use the middle region of the thin-disk model for the surface mass density (for $r \gg r_g$) [65]:

$$\sigma(r) \simeq \frac{10^{-17} M}{r_g^2} \left(\frac{0.01}{\alpha_{\rm disk}}\right)^{\frac{4}{5}} \left(\frac{L}{L_{\rm edd}}\right)^{\frac{3}{5}} \left(\frac{M}{M_\odot}\right)^{\frac{6}{5}} \left(\frac{r}{r_g}\right)^{-\frac{3}{5}}, \quad (36)$$

where $L \lesssim L_{\rm edd}$ is the disk luminosity and $\alpha_{\rm disk} = 0.01$–0.1 characterizes the disk properties; we conservatively use $\alpha_{\rm disk} = 0.01$ and $L = L_{\rm edd}$ in our estimates. Even maximally accreting disks contain a tiny amount of mass, and the effect on the axion cloud is further suppressed by the small height of the disk, $z(r) \simeq 10^{-2} r$ [65].

To find a bound on α/ℓ, we numerically evaluate Eq. (31) using potential perturbation sourced by Eq. (36). Of course only nonuniformities in the disk contribute to the mixing of different levels and the fractional mass in a given mode is even smaller, but to avoid model dependence of the disk substructure, we conservatively take the entire mass of the disk to be concentrated in a spherical harmonics mode that induces mixing of a given SR mode with the fastest-dumping mode. The scenario with the biggest ratios of $\Gamma_{\rm dump}/\Gamma_{\rm sr}$ (thus giving the most stringent bounds) is mixing with the rapidly decaying $\ell' = m' = 0$ mode, followed by the $m' = -m, \ell' = \ell$ mode.

In Fig. 12 we show the resulting bound for the axion clouds of different levels. We emphasize that these are upper bounds on the region affected by the accretion disk. We see that for stellar BHs, the disk constraint on α/ℓ is weaker than that from the companion star. The disks of SMBHs are fractionally smaller in extent, but disk density grows quickly with the BH mass, so the effect of accretion disks around SMBHs is relatively larger. The higher-ℓ levels are more affected by the accretion disk since their superradiance rates are increasingly smaller than the dumping rate of the $\ell' = m' = 0$ level. However, the superradiance time for these levels becomes long and limited by other factors, so they are not relevant for the limits or signals we consider; in agreement with numerical results in [43] the relevant time scale is ~100 SR times. In sum, even with very conservative assumptions, the effect of the accretion disk on the axion cloud does not constrain parameter space where the effect of superradiance is relevant.

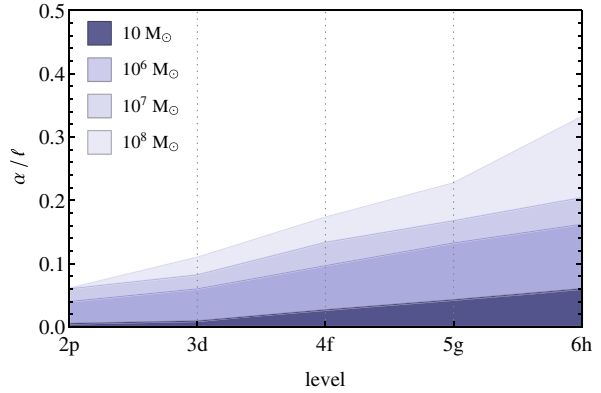

FIG. 12 (color online). Values of α/ℓ for different levels (x-axis) affected by the gravitational potential of the accretion disk. For each level, we assume the entire mass distribution conspires to form the angular mode causing the most dangerous mixing between superradiant and dumping modes. For comparison, the affected range from companion stars for stellar BHs is $\alpha/\ell < 0.05$.

VI. SUMMARY

Advanced LIGO and VIRGO will soon start their science runs, and with the help of the process known as black hole superradiance, they will be the first experiments with potential to discover the QCD axion with decay constants above the grand unification scale. Superradiance fills levels of the gravitational atom formed by the black hole and the axion, creating a macroscopic cloud of axions with large occupation number. Advanced LIGO will be sensitive to gravitational wave radiation from axion annihilations (for Planck-scale QCD axions) and axion transitions between levels (for grand unification scale QCD axions). Advanced VIRGO has similar sensitivity.

Both signals are monochromatic and last dozens of years or more, with time-dependent intensity and frequency drift of 10^{-11} Hz/s or less. These signals are distinct from monochromatic radiation from rapidly spinning asymmetric neutron stars, which have negative frequency drifts following the stars' spin-down rate, while both transition and annihilation signals have frequency drifts anticorrelated in time with the signal intensity.

We extrapolate the current LIGO run's monochromatic search [21] to aLIGO sensitivities, and we estimate that aLIGO should expect up to $\mathcal{O}(1)$ persistent events from axion transitions around stellar black holes. Since the signal lasts longer than the duration of the experiment, this event estimate for transitions could be interpreted as the probability of observing the axion at aLIGO.

For axion annihilations, the optimal reach of aLIGO corresponds to BHs near $30 M_\odot$ in mass for which very little is known. If we extrapolate measured stellar BH distributions to higher masses, we expect thousands of events at aLIGO for axions around 6×10^{-13} eV in mass. Part of the parameter space where annihilations give appreciable event rates is disfavored by BH spin measurements, and in the event that aLIGO does not observe a signal, the resulting limits would provide a cross-check on the spin measurement constraints.

Both axion transitions and annihilations provide the opportunity to discover the QCD axion within a few years' time through its gravitational coupling. Future GW observatories such as the Einstein Telescope may reach a factor of 10 further in sensitivity than aLIGO [67] and detect a factor of 10 or more events than our Advanced LIGO estimates.

A focused search on point sources may also be promising. In particular, annihilation signals from nearby fast-spinning BHs such as those in Table III can probe axion masses of $\mu_a > 10^{-11}$ eV; however, given the age of the

TABLE V. Estimated event rates for transition and annihilation signals at aLIGO and eLISA detectors, if there exists an axion with mass that falls in the sensitive bands of the detectors. These values are simplified following the LIGO event estimation method [22] by assuming that all stellar (supermassive) black holes have mass $10M_\odot$ ($10^6/10^7 M_\odot$), except for the $30M_\odot$ value: we take 10^{-3} of stellar black holes to have this mass. We take into account spin and distance distributions of black holes.

GW signal source	M	$N_{\rm low}$	$N_{\rm re}$	$N_{\rm high}$	f(Hz)
$6g \to 5g$ transition	$10M_\odot$	0.01	0.1	0.5	30
$2p$ annihilation	$30M_\odot^*$	30	300	2000	600
$6g \to 5g$ transition	$10^6 M_\odot$	10^{-4}	0.1	1	3×10^{-4}
$2p$ annihilation	$10^6 M_\odot$	10^{-3}	10	60	2×10^{-2}
$2p$ annihilation	$10^7 M_\odot$	10^{-3}	20	300	2×10^{-3}

BHs and the relatively fast time scales of superradiance and annihilation, we need to be lucky to see such signals. Other point sources worth studying are BHs newly formed after supernovae and binary mergers; the formation events of these BHs can be correlated with the annihilation signals that develop after superradiance has had the time to evolve.

As we can see from Table V and Fig. 9, the prospect for discovery of much lighter axions (between 10^{-19} and 10^{-16} eV) is also promising through the annihilation signal around supermassive BHs at future lower-frequency GW observatories such as eLISA and AGIS. We expect to see up to 10^3 annihilation events, with a large uncertainty. Level transition signals from supermassive black holes would mostly come from BHs with masses below $10^5 M_\odot$. Very little is known about BHs in this mass range, but our estimate in Table V shows that events can also be observed. Our SMBH event rates have a very large uncertainty due to unknown spin distributions and astrophysical uncertainties in the SMBH environment.

One signature we have not explored in detail is GW emission from bosenovae, the collapse of the cloud under its self-interaction, relevant for bosons with self-interaction stronger than that of the QCD axion. Rates for bosenova events are difficult to estimate because the shape and frequency of the signal are sensitive to the dynamics of cloud collapse. This is a particularly interesting avenue for future numerical studies, since the signal has promising amplitude and a distinctive time profile.

The range of axion masses probed by GW detectors is already constrained by black hole spin measurements. For supermassive BHs, these measurements are less reliable given the uncertainties in the spin measurement method as well as the infall rates of compact objects. For stellar BHs, spin measurements are confirmed by two independent techniques, and the environment of the BH is well known in the relevant cases. This makes the exclusion of 6×10^{-13} eV $< \mu_a < 2 \times 10^{-11}$ eV quite robust. This bound is taken into account in our conclusions for the discovery potential of aLIGO.

Astrophysical black hole superradiance diagnoses the presence of light axions in the theory independently of their cosmic evolution and abundance. We focus on the QCD axion in this paper, but the above discussion can be generalized to all spin-0 bosons with weak self-coupling since gravity is the only interaction required. Effects we discussed can also be extended to light spin-1 particles, although further study, in particular of their superradiance rate, is needed.

Throughout this paper, we make several assumptions regarding BH mass and spin distributions; these assumptions lead to the range of event rate expectations for the different signatures presented in Figs. 5, 7, 9, and Table V. Most of the extended range come from the uncertainties in the expected spin distributions; this is especially true for SMBHs since their spin depends on their integrated history which is unknown. Future measurements will shed light on these distributions and will narrow the range presented. Uncertainties due to BH mass distributions are less significant; using different BH mass distributions presented in the literature makes $\mathcal{O}(1)$ difference in the event rate, an uncertainty dominated by large uncertainties in the spin distribution. For stellar BHs annihilation signals, the range of accessible axion masses depends on the tail of the BH mass distribution; we model this uncertainty by imposing a range of upper bounds on the BH mass.

We also use several approximations in our GW power calculations; we expect that our analytic approximations for the GW power calculation are sufficient at this stage. As shown in numerical studies [68], relativistic effects are important for annihilation signals, but our use of the flat space approximation consistently underestimates the power of the signal compared to numerical results even at large values of α/ℓ. We thus consider this approach conservative and appropriate given the large astrophysical uncertainties. For transitions, the signal arises from quadrupole radiation, and deviations from our estimates at the large α/ℓ regime should be at the $\mathcal{O}(1)$ level. Full numerical studies to take into account higher-order corrections and nonlinear effects would be required for further analysis and in the event that a candidate signal is discovered. Numerical studies are also indispensable in the study of the bosenova effect.

The work presented above shows that the imminent discovery of gravitational waves not only gives us a chance to study the properties of black holes but also has the potential to diagnose the presence of new particles. The prospects for discovery are exciting, and our work may only be scratching the surface of the rich phenomena of black hole superradiance.

ACKNOWLEDGMENTS

We are grateful to Tom Abel, Kipp Cannon, Savas Dimopoulos, Sergei Dubovsky, Peter Graham, Junwu Huang, John March-Russell, Joshua Smith, Ken Van Tilburg, and Natalia Toro for many useful comments and

discussions. We especially thank Robert Wagoner for his patience and enthusiasm in helping us learn about black holes. A. A. would like to express her appreciation to Gabriela Gonzalez and Xavier Siemens for extremely useful discussions. A. A. also extends her gratitude to Luis Lehner both for physics discussions and for introducing her to LIGO experimentalists. We thank the CERN Theory Group for their hospitality during the completion of this work. This research was supported in part by Perimeter Institute for Theoretical Physics. Research at Perimeter Institute is supported by the Government of Canada through Industry Canada and by the Province of Ontario through the Ministry of Economic Development & Innovation. This work was supported in part by ERC Grant BSMOXFORD No. 228169. M. B. is supported in part by the Stanford Graduate Fellowship. X. H. is supported in part by the NSF Graduate Research Fellowship under Grant No. DGE-1147470.

APPENDIX A: GRAVITATIONAL WAVE POWER CALCULATION

To calculate the transition rate Γ_t and annihilation rate Γ_a (Secs III A and III B) we make two approximations here as in [4]: we use the flat space formula for the gravitational wave flux and the hydrogen wave functions for the axion wave functions, both of which are valid since the cloud is localized far away from the BH horizon. Further numerical study would be of interest.

For source stress-energy tensor decomposed as

$$T_{\mu\nu} = \sum_{\omega} e^{-i\omega t} T_{\mu\nu}(\omega, \vec{\mathbf{x}}) + \text{c.c.}, \tag{A1}$$

the power per solid angle emitted in a direction $\hat{\mathbf{k}}$ is [69]

$$\frac{dP}{d\Omega} = \sum_{\omega} \frac{G_N \omega^2}{\pi} \Lambda_{ijlm} T^{ij}(\omega, \vec{\mathbf{k}}) T^{lm*}(\omega, \vec{\mathbf{k}}), \tag{A2}$$

where $\vec{\mathbf{k}}^2 = \omega^2$,

$$\Lambda_{ijlm} = P_{mi}P_{jl} - \frac{1}{2}P_{ji}P_{ml}, \qquad P_{ij} = \delta_{ij} - \frac{k_i k_j}{k^2}, \tag{A3}$$

and T_{ij} is the Cartesian spatial component of the Fourier transform

$$T_{\mu\nu}(\omega, \vec{\mathbf{k}}) = \int d^3\vec{\mathbf{x}} e^{-i\vec{\mathbf{k}}\cdot\vec{\mathbf{x}}} T_{\mu\nu}(\omega, \vec{\mathbf{x}}). \tag{A4}$$

We use indices $i, j, \ldots$ to denote Cartesian spatial coordinates for the rest of this section.

We start with the classical axion field,

$$\phi(r,\theta,\varphi) = \sum_{n,l,m} e^{-i\omega_n t} \sqrt{\frac{N_{nlm}}{2\mu_a}} \Psi_{nlm}(r,\theta,\varphi) + \text{c.c.}, \tag{A5}$$

where N_{nlm} is the occupation number and Ψ_{nlm} is the normalized hydrogen wave function for the (n, l, m) level with energy ω_n [Eq. (3)], with stress energy tensor

$$T_{\mu\nu} = \nabla_\mu\phi\nabla_\nu\phi - g_{\mu\nu}\left(\frac{1}{2}\nabla_\rho\phi\nabla^\rho\phi + V(\phi)\right). \tag{A6}$$

In the Minkowski metric the spatial part of the second term is proportional to δ_{ij} and does not contribute to Eq. (A2); therefore the Cartesian spatial component is

$$T_{ij}(r,\theta,\varphi) = \nabla_i\phi\nabla_j\phi, \tag{A7}$$

where

$$\nabla_i = \frac{1}{r}\begin{pmatrix} r\cos\varphi\sin\theta & \cos\theta\cos\varphi & -\csc\theta\sin\varphi \\ r\sin\theta\sin\varphi & \cos\theta\sin\varphi & \cos\varphi\csc\theta \\ r\cos\theta & -\sin\theta & 0 \end{pmatrix}\begin{pmatrix} \partial_r \\ \partial_\theta \\ \partial_\varphi \end{pmatrix}. \tag{A8}$$

Decomposing (A7), we identify terms in the expansions

$$\begin{aligned} T_{ij}(r,\theta,\varphi)|_{\text{ann}} &\equiv T_{ij}(\omega_n + \omega_n', r, \theta, \varphi) \\ &= e^{i(\omega_n+\omega_n')t}\frac{(N_{nlm}N_{n'l'm'})^{\frac{1}{2}}}{2\mu_a} \\ &\quad\times(\nabla_i\Psi_{nlm})(\nabla_j\Psi_{n'l'm'}) \end{aligned} \tag{A9}$$

as the GW source from annihilation of two axions from levels (n, l, m) and (n', l', m'), and

$$\begin{aligned} T_{ij}(r,\theta,\varphi)|_{\text{trans}} &\equiv T_{ij}(\omega_n - \omega_n', r, \theta, \varphi) \\ &= e^{i(\omega_n-\omega_n')t}\frac{(N_{nlm}N_{n'l'm'})^{\frac{1}{2}}}{2\mu_a}(\nabla_i\Psi_{nlm}) \\ &\quad\times(\nabla_j\Psi^*_{n'l'm'}) + \text{c.c.} \end{aligned} \tag{A10}$$

as the GW source from transition from levels (n, l, m) to (n', l', m'). To calculate the GW power, we use Eqs. (A9) and (A10) and Fourier transform to momentum space,

$$\begin{aligned} T_{ij}(\omega,\theta_k,\varphi_k) = \int & dr d\theta d\varphi r^2 \sin\theta \\ &\times\sum_{l,m} 4\pi(-i)^l j_l(\omega r) Y^*_{lm}(\theta,\varphi) \\ &\times Y_{lm}(\theta_k,\varphi_k) T_{ij}(\omega, r, \theta, \varphi), \end{aligned} \tag{A11}$$

TABLE VI. Analytic expressions for GW power from axion annihilations, with $m = l$. For brevity, we expand in α for higher l levels, though the first few higher-order terms are comparable in magnitude.

Level	$(\mathrm{d}P/\mathrm{d}\Omega)N^{-2}$
$2p$	$\frac{\alpha^{18}G_N(6\alpha^3+40\alpha-3(\alpha^2+4)^2\tan^{-1}(2/\alpha))^2(28\cos 2\theta_k+\cos 4\theta_k+35)}{2^{24}\pi(\alpha^2+4)^4 r_g^4}$
$3d$	$\frac{\alpha^{20}G_N\sin^4\theta_k(28\cos 2\theta_k+\cos 4\theta_k+35)}{2^4 3^{16}\pi r_g^4}+\cdots$
$4f$	$\frac{\alpha^{24}G_N\sin^8\theta_k(28\cos 2\theta_k+\cos 4\theta_k+35)}{5^{-2}2^{24}\pi r_g^4}+\cdots$

TABLE VII. Analytic expressions for GW power from transitions. Higher order terms in α are smaller by a factor of 10 or more.

Level	$(\mathrm{d}P/\mathrm{d}\Omega)N_{nlm}^{-1}N_{n'l'm'}^{-1}$
$6g \to 5g$	$\frac{2^{28}3^4 5^5\alpha^{12}G_N\sin^4\theta_k}{11^{22}\pi r_g^4}+\cdots$
$7h \to 6h$	$\frac{2^{31}3^7 5^2 7^6\alpha^{12}G_N\sin^4\theta_k}{13^{26}\pi r_g^4}+\cdots$
$5f \to 4f$	$\frac{2^{22}5^2\alpha^{12}G_N\sin^4\theta_k}{3^{34}\pi r_g^4}+\cdots$

where j_l are the spherical Bessel functions and Y_{lm} are the spherical harmonics.

We then plug Eq. (A11) into Eq. (A2) to calculate the differential power. To calculate the annihilation and transition rates, we use

$$\Gamma_a \equiv \frac{\int \mathrm{d}\Omega(\mathrm{d}P/\mathrm{d}\Omega)|_{\mathrm{ann}}}{2\omega N^2}, \quad \text{and} \quad \Gamma_t \equiv \frac{\int \mathrm{d}\Omega(\mathrm{d}P/\mathrm{d}\Omega)|_{\mathrm{tr}}}{\omega N N'}, \tag{A12}$$

respectively. We list the differential power for the most relevant annihilations and transitions in Tables VI and VII.

For the $2p$ level, we find a cancellation in the leading α term because our calculation is performed in the flat space approximation. The leading α term is restored if we take into account the first-order corrections due to the BH gravitational potential, which agrees with the calculation in the Schwarzschild background in [43] and the numerical result in [68]; we thank the authors of [68] for clarifying this issue. Our calculation, which we adopt throughout this paper, should thus be considered as a lower bound on the GW production.

APPENDIX B: REACH OF GW EXPERIMENTS

For each mass μ_a, we calculate the reach to a black hole of mass M that optimizes the signal strength and with spin $a_* = 0.9$ or $a_* = 0.99$. In each plot, the top axis shows the corresponding GW frequency. We assume a maximally filled axion cloud for annihilations and a peak transition strain for $6g \to 5g$ transitions.

We plot the reach of aLIGO [19], eLISA [29], and AGIS [31] based on their design strain sensitivities, using 121 segments of 250 hr integration time and a trials factor of 10 as described in Sec. III. We extrapolate the AGIS sensitivity to lower frequencies (dashed curve) assuming the same frequency dependence of the noise floor as that at mHz.

We indicate with vertical lines when the optimal BH masses are heavier than $100M_\odot$ and lighter than $3M_\odot$ (stellar BHs), or heavier than $10^9 M_\odot$ and lighter than $10^6 M_\odot$ (SMBHs). Outside of this range, there are few observations to guide estimates of BH mass distributions.

The shaded regions are disfavored by the observation of rapidly spinning black holes for bosons with coupling equal to that of the QCD axion (light gray) or stronger (dark gray) (see section IV).

APPENDIX C: EVENT RATE CALCULATION

We calculate the event rates by incorporating the various astrophysical distributions:

$$\begin{aligned}\text{Number of Events} \equiv & \int_0^1 \mathrm{d}a_* P(a*) \int_0^\infty \mathrm{d}r P(r) \\ & \times \int_0^{M_{\max}} \mathrm{d}M P(M) \\ & \times \tau_{\mathrm{sig}}(M, a_*, r) \times \mathrm{BHFR}, \end{aligned} \tag{C1}$$

where BHFR is the black hole formation rate, $P(a_*)$, $P(M)$, $P(r)$ are the normalized probability distributions to find a black hole with spin a_*, mass M, and distance r away, and $\tau_{\mathrm{sig}}(M, a_*, r)$ is the duration for which the GW signal from a BH with mass M, spin a_*, and distance r away is above the noise threshold of the detector.

1. Stellar black hole distributions

Mass distribution.—We quantify the probability of finding a black hole of a certain mass by using an exponential fit to current data, which is found to be the best fit out of five functional forms (Table 7 in [23]):

$$P(M) = M_0^{-1} e^{\frac{M_{\min}}{M_0}} e^{-\frac{M}{M_0}}. \tag{C2}$$

Here $M_{\min} = 5.3^{+0.9}_{-1.2} M_\odot$ is the minimum BH mass which can be formed from stellar collapse and $M_0 = 4.7^{+3.2}_{-1.9} M_\odot$ sets the width of the distribution (Table 5 in [23]). We verified that the uncertainty in the range of values we use for the exponential fit is larger than the variation with respect to the second best-fit function ("double Gaussian").

In computing the event rates for transitions, we use $M_{\min} = 4.1 M_\odot$, within the experimental fit and above theoretical maximum of neutron star mass, $\lesssim 2.9 M_\odot$ [70]; lowering $M_{\min}$ shifts the event distribution to higher axion masses. Larger values of M_0 give wider distributions.

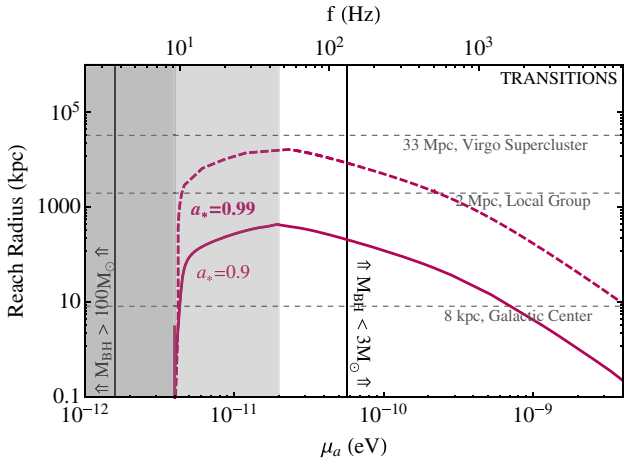

FIG. 13 (color online). aLIGO reach for a black hole–axion atom currently undergoing the $6g \to 5g$ transition as a function of the axion mass at the maximum rate for a black hole spin of $a_* = 0.9$ (solid) and $a_* = 0.99$ (dashed).

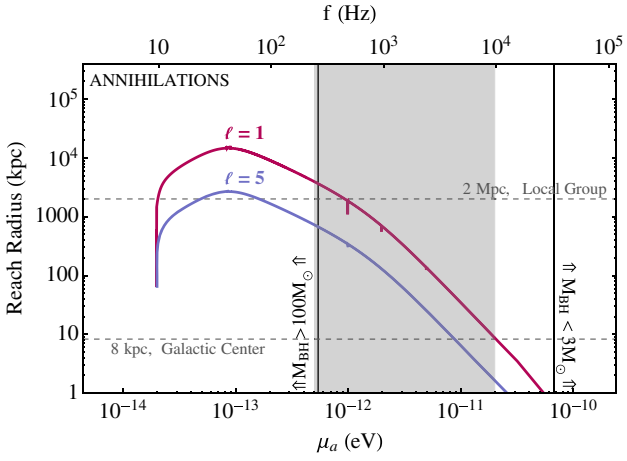

FIG. 15 (color online). aLIGO reach as a function of the axion mass for an axion cloud currently undergoing annihilations at the maximum rate $a_* = 0.9$ for ($\ell = 1$ and 5, $n = \ell + 1$).

We use the following three values for M_0 parameter for the three bands in Fig. 5:

(i) Narrow: $M_0 = 2.8M_\odot$
(ii) Intermediate: $M_0 = 4.7M_\odot$
(iii) Wide: $M_0 = 7.9M_\odot$.

We expect the narrower distribution is more accurate for young BHs because some larger masses are attained by accretion.

In annihilation event rates (Fig. 7), we vary M_0 as part of our pessimistic and optimistic estimates, respectively, since the aLIGO event rate is sensitive to the exponential tail of massive BHs. We plot three bands in Fig. 7 corresponding to different hard cutoff $M_{\max}$ to further account for this uncertainty:

(i) Narrow: $M_{\max} = 30M_\odot$
(ii) Intermediate: $M_{\max} = 80M_\odot$
(iii) Wide: $M_{\max} = 160M_\odot$.

Within each band, we fix $M_{\min} = 4.1M_\odot$ and vary M_0 from 2.8 to $7.9M_\odot$ with the central curves given by $M_0 = 4.7M_\odot$. Not much is known about the heavier stellar BHs: the heaviest known stellar BH has mass $32.7 \pm 2.6M_\odot$ [71], while theoretical modeling of BH formation from a single star can accommodate maximum stellar BH mass of 30–$80M_\odot$ depending on the metallicity of the environment [72].

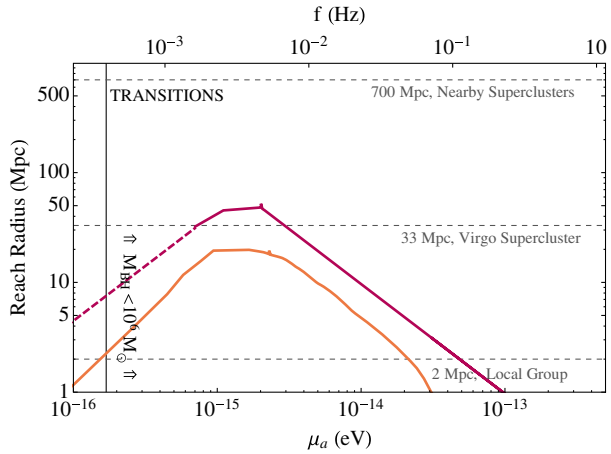

FIG. 14 (color online). AGIS (red/dark gray) and eLISA (orange/light gray) reach as a function of the axion mass for a black hole–axion atom currently undergoing the $6g \to 5g$ transition at the maximum rate for BHs with spin $a_* = 0.99$. For $a_* = 0.9$ the reach is decreased by a constant factor ~50 as in Fig. 13, making the signal from extragalactic BHs barely observable.

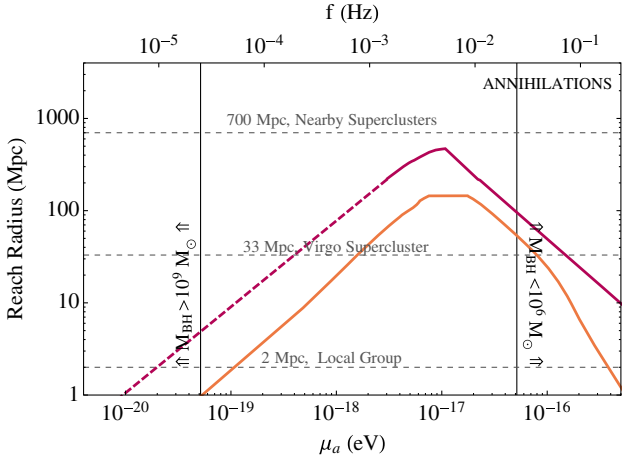

FIG. 16 (color online). AGIS (red/dark gray) and eLISA (orange/light gray) reach as a function of the axion mass for a black hole atom currently undergoing $2p$ annihilations at the maximum rate for BH spin $a_* = 0.99$. For $a_* = 0.9$ the reach is decreased by a constant factor ~50 as in Fig. 13; for $a_* = 0.7$ the reach decreases below 1 Mpc for both experiments, making the signal unobservable for extragalactic sources.

Spin distribution.—The measured distribution is peaked at high spins (30% above 0.8) which we take as a realistic estimate. We consider 90% above 0.8 as optimistic—a high birth spin is likely since the progenitor star has to lose a lot of angular momentum to collapse to the small BH, and in the case a light boson is present, some observed BHs would have spun down since their birth. We take a flat initial spin distribution as pessimistic.

Formation rate.–Barring rare violent events (e.g. neutron star–BH or BH-BH mergers, $<10^{-2}$ per century in the Milky Way [22]), event probability is proportional to the BH birth rate. Core collapse supernovae rates are estimated to be 1.9 ± 1.1 per century [24,25]. The fraction of supernovae that form black holes is estimated to be 15% in metal-rich stars like the Sun [26] with a large uncertainty. Based on average metallicities today, $20 \pm 10\%$ [26,73] of supernovae form BHs. This leads us to an optimistic value of 0.9, realistic of 0.38, and pessimistic of 0.08 BHs formed per century.

Violent BH formation may impede superradiant growth and delay the signal until a more uniform accretion disk forms; our conclusions are unaffected by delays less than a Gyr, and the unlikely case of delays >5 Gyr would increase the signal by a factor of 3 due to higher star formation rates [74].

Distance distribution.—We assume the distance distribution of BHs in the Milky Way is proportional to the stellar distribution [27]. Outside of our Galaxy we scale the number of BHs in our Galaxy N_{MW} by the blue luminosity distribution in [28], which asymptotes to $N_{\rm bh} = 0.0042 N_{\rm MW} (r/{\rm Mpc})^3$ at distances $r > 30$ Mpc.

2. Supermassive black hole distributions

Mass and distance distribution.—Supermassive BHs are generally understood to reach their mass through accretion, with most BHs with mass 10^6–$10^7 M_\odot$ and a tail extending to $10^{10} M_\odot$. We use the distributions of [38,39], which give a total amount of mass in SMBHs as $\rho_{\rm bh} = (3.2\text{–}5.4) \times 10^5 M_\odot {\rm Mpc}^{-3}$, or about one $10^7 M_\odot$ BH per MW-type galaxy; we extrapolate down to $10^{5.5} M_\odot$ from $10^6 M_\odot$. We scale this distribution according to [28] at distances closer than 30 Mpc.

Spin distribution.—The biggest uncertainty for event rates is due to the unknown spin distribution of SMBHs. Some simulations of thin disk accretion find that 70% of SMBHs are maximally rotating [40]. Black holes quickly spin up to maximal spin, where maximal is less than 1 due to counteracting torques from either radiation emitted from the disk and absorbed by the BH ($a_*^{\rm max} = 0.998$) [75], or magnetic fields transporting angular momentum away from the BH ($a_*^{\rm max} = 0.93$) in simulations of thick disk models [76]. We use 70% of SMBHs with spins $a_* \geq 0.93$ as an optimistic estimate. For a pessimistic estimate, we use the chaotic accretion model [42] which gives low spin $a_* = 0.2 \pm 0.2$; this leads to less than 10^{-2} events but is also disfavored by measurements of many rapidly spinning BHs. Merger dominated models give $a_* \sim 0.7$ [77]. For a realistic estimate we use the hybrid model of [41] where 70% of SMBHs have spins $a_* \geq 0.7$ with 50% above 0.9 (for BHs below $10^7 M_\odot$ in mass, which are the ones contributing dominantly to the signal).

[1] R. Penrose, Riv. Nuovo Cimento **1**, 252 (1969).
[2] T. Zouros and D. Eardley, Ann. Phys. (N.Y.) **118**, 139 (1979); S. Detweiler, Phys. Rev. D **22**, 2323 (1980); A. B. Gaina and I. Ternov, Sov. Phys. J. **31**, 830 (1988).
[3] A. Arvanitaki, S. Dimopoulos, S. Dubovsky, N. Kaloper, and J. March-Russell, Phys. Rev. D **81**, 123530 (2010).
[4] A. Arvanitaki and S. Dubovsky, Phys. Rev. D **83**, 044026 (2011).
[5] V. L. Ginzburg, Phys. Usp. **39**, 973 (1996).
[6] J. Bekenstein and M. Schiffer, Phys. Rev. D **58**, 064014 (1998).
[7] Y. B. Zel'Dovich, Sov. JETP Lett. **14**, 180 (1971); Y. B. Zel'dovich, L. V. Rozhanskii, and A. A. Starobinskii, Radiophys. Quantum Electron. **29**, 761 (1986).
[8] R. Peccei and H. R. Quinn, Phys. Rev. Lett. **38**, 1440 (1977); S. Weinberg, Phys. Rev. Lett. **40**, 223 (1978); F. Wilczek, Phys. Rev. Lett. **40**, 279 (1978).
[9] A. Arvanitaki, J. Huang, and K. Van Tilburg, Phys. Rev. D **91**, 015015 (2015).
[10] J. Hewett, H. Weerts, R. Brock, J. Butler, B. Casey *et al.*, arXiv:1205.2671.
[11] G. M. Harry (LIGO Scientific Collaboration), Classical Quantum Gravity **27**, 084006 (2010).
[12] T. Accadia, F. Acernese, F. Antonucci, P. Astone, G. Ballardin *et al.*, Classical Quantum Gravity **28**, 114002 (2011).
[13] S. R. Dolan, Phys. Rev. D **76**, 084001 (2007).
[14] P. Pani, V. Cardoso, L. Gualtieri, E. Berti, and A. Ishibashi, Phys. Rev. D **86**, 104017 (2012); J. G. Rosa and S. R. Dolan, Phys. Rev. D **85**, 044043 (2012).
[15] E. A. Donley, N. R. Claussen, S. L. Cornish, J. L. Roberts, E. A. Cornell, and C. E. Wieman, Nature (London) **412**, 295 (2001).
[16] S. Dubovsky and V. Gorbenko, Phys. Rev. D **83**, 106002 (2011).
[17] H. Yoshino and H. Kodama, Prog. Theor. Phys. **128**, 153 (2012).
[18] R. Brito, V. Cardoso, and P. Pani, arXiv:1501.06570.

[19] J. Aasi *et al.* (LIGO Scientific Collaboration, Virgo Collaboration), arXiv:1304.0670.
[20] X. Siemens (private communication).
[21] J. Aasi, J. Abadie, B. Abbott, R. Abbott, T. Abbott, M. Abernathy, T. Accadia, F. Acernese, C. Adams, T. Adams *et al.*, Phys. Rev. D **87**, 042001 (2013).
[22] J. Abadie *et al.* (LIGO Scientific Collaboration, Virgo Collaboration), Classical Quantum Gravity **27**, 173001 (2010).
[23] W. M. Farr, N. Sravan, A. Cantrell, L. Kreidberg, C. D. Bailyn, I. Mandel, and V. Kalogera, Astrophys. J. **741**, 103 (2011).
[24] R. Diehl, H. Halloin, K. Kretschmer, G. G. Lichti, V. Schoenfelder *et al.*, Nature (London) **439**, 45 (2006).
[25] N. Prantzos and S. Boissier, Astron. Astrophys. **406**, 259 (2003).
[26] A. Heger, C. Fryer, S. Woosley, N. Langer, and D. Hartmann, Astrophys. J. **591**, 288 (2003).
[27] S. Sale, J. Drew, C. Knigge, A. Zijlstra, M. Irwin, R. Morris, S. Phillipps, J. Drake, R. Greimel, Y. Unruh *et al.*, Mon. Not. R. Astron. Soc. **402**, 713 (2010).
[28] R. K. Kopparapu, C. Hanna, V. Kalogera, R. O'Shaughnessy, G. Gonzalez, P. R. Brady, and S. Fairhurst, Astrophys. J. **675**, 1459 (2008).
[29] P. Amaro-Seoane, S. Aoudia, S. Babak, P. Binetruy, E. Berti *et al.*, Classical Quantum Gravity **29**, 124016 (2012).
[30] P. McNamara, in The 40th COSPAR Scientific Assembly, Moscow, Russia, 2014, Abstract No. H0.5-2-14., COSPAR Meeting, (2014), Vol. **40**, p. 2051.
[31] S. Dimopoulos, P. W. Graham, J. M. Hogan, M. A. Kasevich, and S. Rajendran, Phys. Rev. D **78**, 122002 (2008).
[32] J. M. Hogan and M. A. Kasevich, arXiv:1501.06797.
[33] P. W. Graham, J. M. Hogan, M. A. Kasevich, and S. Rajendran, Phys. Rev. Lett. **110**, 171102 (2013).
[34] E. Fermi and G. E. Uhlenbeck, Phys. Rev. **44**, 510 (1933).
[35] I. Khabibullin and S. Sazonov, Mon. Not. R. Astron. Soc. **444**, 1041 (2014).
[36] G. Brown and H. Bethe, Astrophys. J. **423**, 659 (1994).
[37] D. R. Pasham, T. E. Strohmayer, and R. F. Mushotzky, Nature (London) **513**, 74 (2014).
[38] B. C. Kelly and A. Merloni, Adv. Astron. **2012**, 970858 (2012).
[39] F. Shankar, D. H. Weinberg, and J. Miralda-Escudé, Astrophys. J. **690**, 20 (2009).
[40] M. Volonteri, P. Madau, E. Quataert, and M. J. Rees, Astrophys. J. **620**, 69 (2005).
[41] A. Sesana, E. Barausse, M. Dotti, and E. M. Rossi, Astrophys. J. **794**, 104 (2014).
[42] A. R. King, J. E. Pringle, and J. A. Hofmann, Mon. Not. R. Astron. Soc. **385**, 1621 (2008).
[43] R. Brito, V. Cardoso, and P. Pani, arXiv: 1411.0686.
[44] J. E. McClintock, R. Narayan, and J. F. Steiner, Space Sci. Rev. **183**, 295 (2014).
[45] C. S. Reynolds, Space Sci. Rev. **183**, 277 (2014).
[46] J. M. Bardeen, W. H. Press, and S. A. Teukolsky, Astrophys. J. **178**, 347 (1972).
[47] J. McClintock, R. Narayan, L. Gou, R. Penna, and J. Steiner, AIP Conf. Proc. **1248**, 101 (2010).
[48] J. Miller, C. Reynolds, A. Fabian, G. Miniutti, and L. Gallo, Astrophys. J. **697**, 900 (2009).
[49] A. Fabian, M. Rees, L. Stella, and N. E. White, Mon. Not. R. Astron. Soc. **238**, 729 (1989).
[50] C. S. Reynolds, Classical Quantum Gravity **30**, 244004 (2013).
[51] D. Budker, P. W. Graham, M. Ledbetter, S. Rajendran, and A. Sushkov, Phys. Rev. X **4**, 021030 (2014).
[52] J. E. McClintock, R. Shafee, R. Narayan, R. A. Remillard, S. W. Davis, and L.-X. Li, Astrophys. J. **652**, 518 (2006).
[53] J. Steiner (private communication).
[54] L. Gou, J. E. McClintock, M. J. Reid, J. A. Orosz, J. F. Steiner, R. Narayan, J. Xiang, R. A. Remillard, K. A. Arnaud, and S. W. Davis, Astrophys. J. **742**, 85 (2011).
[55] W. Pietsch, F. Haberl, M. Sasaki, T. Gaetz, P. Plucinsky, P. Ghavamian, K. Long, and T. Pannuti, Astrophys. J. **646**, 420 (2006).
[56] L. Gou, J. E. McClintock, J. Liu, R. Narayan, J. F. Steiner, R. A. Remillard, J. A. Orosz, S. W. Davis, K. Ebisawa, and E. M. Schlegel, Astrophys. J. **701**, 1076 (2009).
[57] L. Ruhlen, D. Smith, and J. Swank, Astrophys. J. **742**, 75 (2011).
[58] B. Willems, M. Henninger, T. Levin, N. Ivanova, V. Kalogera, K. McGhee, F. X. Timmes, and C. L. Fryer, Astrophys. J. **625**, 324 (2005).
[59] M. Mendez, T. Belloni, and M. Van der Klis, Astrophys. J. **499**, L187 (1998).
[60] L. Gou, J. E. McClintock, R. A. Remillard, J. F. Steiner, M. J. Reid, J. A. Orosz, R. Narayan, M. Hanke, and J. García, Astrophys. J. **790**, 29 (2014).
[61] T.-W. Wong, F. Valsecchi, T. Fragos, and V. Kalogera, Astrophys. J. **747**, 111 (2012).
[62] M. J. Reid, J. E. McClintock, J. F. Steiner, D. Steeghs, R. A. Remillard, V. Dhawan, and R. Narayan, Astrophys. J. **796**, 2 (2014).
[63] V. Dhawan, I. Mirabel, M. Ribó, and I. Rodrigues, Astrophys. J. **668**, 430 (2007).
[64] D. Steeghs, J. McClintock, S. Parsons, M. Reid, S. Littlefair, and V. S. Dhillon, Astrophys. J. **768**, 185 (2013).
[65] N. Shakura and R. Sunyaev, Astron. Astrophys. **24**, 337 (1973).
[66] S. M. S. Kato and J. Fukue, *Black-hole Accretion Disks* (Kyoto University Press, Kyoto, 1998).
[67] M. Punturo, M. Abernathy, F. Acernese, B. Allen, N. Andersson, K. Arun, F. Barone, B. Barr, M. Barsuglia, M. Beker *et al.*, Classical Quantum Gravity **27**, 194002 (2010).
[68] H. Yoshino and H. Kodama, Prog. Theor. Exp. Phys. **2014**, 43E02 (2014).
[69] S. Weinberg, *Gravitation and Cosmology: Principles and Applications of the General Theory of Relativity* (Wiley, New York, 1972), Chap. 10.
[70] V. Kalogera and G. Baym, Astrophys. J. Lett. **470**, L61 (1996).
[71] J. M. Silverman and A. V. Filippenko, Astrophys. J. Lett. **678**, L17 (2008).
[72] K. Belczynski, T. Bulik, C. L. Fryer, A. Ruiter, F. Valsecchi, J. S. Vink, and J. R. Hurley, Astrophys. J. **714**, 1217 (2010).

[73] W.-Q. Zhang, S. Woosley, and A. Heger, Astrophys. J. **679**, 639 (2008).
[74] R. Bouwens, G. Illingworth, I. Labbe, P. Oesch, M. Trenti *et al.*, Nature (London) **469**, 504 (2011).
[75] K. S. Thorne, Astrophys. J. **191**, 507 (1974).
[76] C. F. Gammie, S. L. Shapiro, and J. C. McKinney, Astrophys. J. **602**, 312 (2004).
[77] E. Berti and M. Volonteri, Astrophys. J. **684**, 822 (2008).